Posiva SKB Report 13
January 2022

Numerical model for the quantification of buffer bentonite mass losses due to expansion, erosion and sedimentation

Arnau Pont
Andrés Idiart

POSIVA OY

Olkiluoto
FI-27160 Eurajoki, Finland
Phone +358 2 8372 31
posiva.fi

SVENSK KÄRNBRÄNSLEHANTERING AB

SWEDISH NUCLEAR FUEL
AND WASTE MANAGEMENT CO

Box 3091, SE-169 03 Solna
Phone +46 8 459 84 00
skb.se

ISSN 2489-2742
Posiva SKB Report 13
SKB ID 1964186
Posiva ID RDOC-105044

January 2022
Updated July 2024

Numerical model for the quantification of buffer bentonite mass losses due to expansion, erosion and sedimentation

Arnau Pont, Andrés Idiart
Amphos 21 Consulting S.L.

The original report, dated January 2022, was found to contain editorial errors which have been corrected in this updated version.

Summary

In this work, the general principles and guidelines presented in Pont et al. (2020) regarding the numerical modelling of bentonite expansion and erosion are further developed. The series of improvements proposed as an extension of the model developed by Neretnieks et al. (2009), Liu et al. (2009) and Moreno et al. (2010) accounting for wall friction and fluid non-linear effects have been implemented in COMSOL Multiphysics and tested with relevant experimental data. Mass losses due to chemical erosion below the Critical Coagulation Concentration (CCC) have also been modelled, as well as the effect of gravity in sloping fractures. The underlying modelling framework is based as much as possible on fundamental physics, in an attempt to avoid resorting to empirical approaches.

The final goal of this study consists in providing a complete computational framework that considers all relevant features of bentonite expansion, erosion, and sedimentation under realistic repository conditions. In the present work, focus is made on understanding, modelling, and quantifying the buffer mass losses due to the presence of intersecting fractures with low salinity groundwaters. In this sense, the effects of mechanical erosion due to shear by seeping water, chemical erosion, and sedimentation due to gravity are analysed. Moreover, the definition of the wall friction term presented in Pont et al. (2020) is associated to the shear resistance of the non-expansive sediment-gel that appears at the bentonite-water interface in cases below CCC and with insufficient supply of divalent ions (Neretnieks and Moreno 2021). This feature is of crucial importance for properly assessing the expansion-erosion equilibrium (pseudo-steady state), which will have a strong influence on the total erosion rate. For this reason, the model has been applied to several small-scale tests including different clay pellet volumes, fracture apertures, initial dry densities, slopes, and flow rates. However, several processes have been left out of the scope. These include (1) clogging caused by accessory minerals or secondary gel, (2) stabilization provided by calcium absorption through ionic exchange, and chemical reactions due to bentonite-groundwater interaction. Solute transport has been reduced to the sodium system, for which the present approach can be considered as conservative. The results show, on one hand, that wall friction limits the expansion of bentonite in scenarios with low fracture flow velocities below CCC, thus limiting the erosion rate as observed in small-scale tests (Schatz et al. 2013). On the other hand, the model also reproduces the degradation of compacted bentonite in sloping 1 mm fractures, and as expected, is not able to predict clogging due to secondary gel formation in 0.1 mm fractures.

Once tested, the model has been applied to realistic repository conditions of the bentonite buffer intersected by a fracture. Again, several flow and fracture configurations have been simulated to provide a preliminary assessment of the long-term integrity when glacial groundwater intrudes the bentonite buffer. The results show that the current model reduces the level of conservatism of the predicted erosion rates for both horizontal and sloping fractures when compared to the KTH model used in Schatz et al. (2013) and the upscaling method presented in Smith et al. (2017).

Sammanfattning

I detta arbete har de allmänna principer och riktlinjer som presenteras i Pont et al. (2020) angående den numeriska modelleringen av bentonitexpansion och erosion vidareutvecklas. De förslag till vidareutveckling av den modell som utvecklades av Neretnieks et al. (2009), Liu et al. (2009) och Moreno et al. (2010) och som hanterar väggfriktion och icke-linjära vätskeeffekter har implementerats i COMSOL Multiphysics och testats med relevanta experimentella data. Massförluster på grund av kemisk erosion för salthalter under den kritiska koaguleringskoncentrationen (CCC) har också modellerats, liksom effekter av gravitation i sluttande sprickor. Det underliggande modelleringsramverket bygger så långt som möjligt på fundamental fysik, i ett försök att undvika att tillgripa empiriska tillvägagångssätt.

Det övergripande målet med denna studie är i att ta fram ett komplett beräkningsramverk som tar hänsyn till alla relevanta egenskaper hos bentonitexpansion, erosion och sedimentation under realistiska förvarsförhållanden.

Detta arbete har fokuserats på att förstå, modellera och kvantifiera massförluster från bufferten orsakade av sprickor med grundvatten som har låg salthalt som är i kontakt med deponeringshålet. I detta sammanhang har effekterna av mekanisk erosion på grund av skjuvning genom strömmande vatten, kemisk erosion och sedimentation orsakad av gravitationen analyseras. Dessutom har definitionen av väggfriktionstermen, som presenterades i Pont et al. (2020), associerats med skjuvmotståndet hos den icke-expansiva sedimentgelen som uppträder vid bentonit-vattengränsytan för fall med koncentrationer under CCC och med begränsad tillgång på tvåvärda joner (Neretnieks och Moreno 2021). Denna egenskap är av avgörande betydelse för att korrekt bestämma expansion-erosion jämvikten (pseudo-steady state), vilken har stort inflytande på den totala erosionshastigheten. Av detta skäl har modellen testats på flera småskaliga tester, med variationer i lerpelletsvolym, volymer, sprickapertur, initial torrdensitet, lutning och flödeshastighet. Det finns dock flera processer som fortfarande inte kan hanteras. Dessa inkluderar (1) igensättning orsakad av accessoriska mineral eller en sekundär gel, (2) stabilisering orsakad av kalciumabsorption genom jonbyte och kemiska reaktioner mellan grundvattnet och bentoniten. Transport av lösta ämnen har reducerats till att bara hantera natriumsystemet, vilket innebär att nuvarande tillvägagångssättet kan betraktas som pessimistiskt med avseende på erosion. Resultaten visar å ena sidan att väggfriktion begränsar expansionen av bentonit i fall med låga flödeshastigheter i sprickor och koncentrationer under CCC. Detta begränsar erosionshastigheten vilket också har observerats i småskaliga tester (Schatz et al. 2013). Å andra sidan, kan modellen också simulera sedimentation av bentonit i sluttande 1 mm sprickor, men kan inte, vilket var förväntat, hantera den sekundära gelbildning som har observerats i 0,1 mm sprickor.

Efter testning har modellen tillämpats på realistiska förvarsförhållanden för en bentonitbuffert i kontakt med en spricka med grundvatten. Flera flödes- och sprickkonfigurationer har simulerats för att ge en preliminär bedömning av den långsiktiga integriteten när utspätt grundvatten kommer i kontakt med en bentonitbuffert. Resultaten visar att den nuvarande modellen minskar nivån av pessimism i beräknade erosionshastigheter för både horisontella och sluttande sprickor jämfört med KTH-modellen som användes används i Schatz et al. (2013) och uppskalningsmetoden som presenteras i Smith et al. (2017).

Tiivistelmä

Tässä työssä on kehitetty edelleen Pont ym. (2020) esittämiä periaatteita liittyen bentoniitin rakotunkeuman ja eroosion numeeriseen mallinnukseen. Neretnieksin ym. (2009), Liu ym. (2009) ja Moreno ym. (2010) kehittämään malliin on esitetty sarja laajennuksia, jotka ottavat huomioon seinämäkitkan ja nesteen epälineaariset vaikutukset. Laajennukset on käyttöönotettu COMSOL Multiphysics -ohjelmassa ja testattu kokeellisen aineiston avulla. Tässä työssä on mallinnettu myös kemiallisen eroosion aiheuttama massahäviö CCC-konsentraatiopistettä (Critical Coagulation Concentration) laimeammissa olosuhteissa sekä otettu huomioon painovoiman vaikutus kaltevissa rakokulmissa. Mallinnuksessa on pyritty hyödyntämään mahdollisimman pitkälle fysiikan perusilmiöitä.

Tämän tutkimuksen tavoitteena on esittää laskennallinen malli, joka ottaa huomioon loppusijoitusolosuhteissa bentoniitin rakotunkeumaan, eroosioon ja sedimentaatioon oleellisimmin vaikuttavat tekijät. Työssä keskitytään puskurin massahäviöiden ymmärtämiseen, mallintamiseen ja kvantifiointiin olosuhteissa, joissa puskuri altistuu laimealle pohjavedelle loppusijoitusreikää leikkaavassa kallioraossa. Vastaavasti virtaavasta laimeasta vedestä johtuvaa kemiallisen eroosion ja sedimentaation aiheuttamaa mekaanista eroosiota analysoitiin tässä työssä. Lisäksi Pont ym. (2020) esittämä seinäkitka kytkeytyy bentoniitti-vesi rajapinnassa olevan paisumattoman sedimenttigeelin leikkauslujuusominaisuuksiin. Tämä koskee tapauksia, joissa kahden arvoisten ionien konsentraatio on alhainen ja liuoksen kokonaisionikonsentraatio on alle CCC-pisteen (Neretnieks ja Moreno 2021). Tämä ominaisuus on ratkaisevan tärkeä todellisen rakotunkeuma-eroosio-tasapainon (pseudo-steady state) määrittämisessä, koska se vaikuttaa kokonaiseroosionopeuteen. Tästä syystä mallia testattiin kokeellisissa pienen mittakaavan keinorakokokeissa. Kokeissa vaihdeltiin bentoniittimäärää, rakoavaumaa, bentoniitin alkutilan kuivatiheyttä, raon kaltevuuskulmaa ja laimean veden virtausnopeutta. Kaikkia prosesseja ei huomioitu kokeellisessa työssä, kuten (1) raon tukkeutumista aksessoristen mineraalien tai sekundäärisen geeliytymisen johdosta, eikä (2) kalsiumin ioninvaihtoreaktion stabiloivaa vaikutusta tai bentoniitti-pohjavesi vuorovaikutuksen aiheuttamien kemiallisten reaktioiden vaikutusta. Liuenneen aineen kulkeutuminen on rajattu tässä työssä yksinkertaiseen natriumionisysteemiin, jota voidaan pitää konservatiivisena lähestymistapana.

Tulokset osoittavat, että seinämäkitka rajoittaa bentoniitin rakotunkeumaa alhaisissa rakovirtausnopeuksissa CCC-konsentraatiopisteen alapuolella. Tämä rajoittaa eroosion nopeutta, kuten pienen mittakaavan kokeissa on havaittu (Schatz ym. 2013). Toisaalta malli toistaa bentoniitin eroosion kaltevissa 1 mm:n rakoavaumissa, mutta ei pysty ennustamaan sekundaarisen geelin aiheuttamaa raon tukkeutumista kapeammassa 0,1 mm:n rakoavaumassa.

Mallia skaalattiin myös todellisiin loppusijoitusolosuhteisiin. Laskennassa tarkasteltiin kallioraon kautta laimeaan jäätikköveteen kosketuksissa olevaa puskuribentoniittia useissa eri virtaus- ja rakokon-figuraatioissa. Tulosten perusteella tässä työssä esitetty malli vähentää arvioitujen eroosionopeuksien konservatiivisuutta horisontaalisissa ja kaltevissa kalliorakosysteemeissä verrattaessa KTH-malliin (Schatz ym, 2013) ja Smith ym. (2017) esittämään skaalausmenetelmään.

Contents

1 Introduction

1.1 Background

In recent years, the mechanisms of bentonite erosion have been intensively investigated to better understand their potential impact on the long-term integrity of the compacted bentonite buffer in the KBS-3 concept over the long term. As part of the EU integrated project BELBaR (Bentonite Erosion: effects on the long-term performance of the engineered Barrier and Radionuclide transport, between 2012 and 2016), several experiments and modelling approaches were conducted and developed. As a result, the erosion models previously used by SKB and Posiva in the initial long-term safety assessments for the final repositories for spent nuclear fuel were further developed and updated. The refined model can be transformed into a relatively simple expression that can be used for quantitative assessments (Neretnieks et al. 2017). However, there are still large uncertainties regarding some of the expansion (or extrusion) and erosion mechanisms, such as gravity, chemical erosion, and friction. These mechanisms still must be properly integrated into a conceptual and computational model.

In this line, the POSKBAR project aims at quantifying the eroded mass loss of bentonite from the buffer triggered by low salinity groundwater below the Critical Coagulation Concentration (CCC) by two means: experimentally with simplified laboratory tests (Schatz et al. 2013, Schatz and Akhanoba 2017 and Appendix D), and numerically with a computational model that overcomes the limitations of the existing approaches. Regarding the latter, Pont et al. (2020) presented several possible solutions to some of the aforementioned uncertainties as a first stage of this work. These included wall friction and viscous effects leading to mechanical erosion. In the present work, these ideas are translated into a numerically robust and tested computational model to be applied to realistic repository conditions. Moreover, the recent work devoted to the experimental analysis of chemical erosion by Posiva (Appendix D) within the Dilbi project has been widely considered in the present report.

For the sake of clarity, a definition of the most relevant concepts related to bentonite-water mixtures is provided next (Neretnieks et al. 2009):

Sheet*:* The smallest building of clay, typically a very thin irregular coin-like sheet, sometimes called lamella, platelet, or flake.

Gel: A dispersion in which the particles cannot move independently of each other. Two main reasons for this are common. Particles are held together by attractive forces. This is the case when they have coagulated in ionic strengths above the critical coagulation concentration. This is called *cohesive* gel. A *repulsive* or *expansive* gel (sometimes referred to as expanding paste in the text) expands until it fills up all the volume available if there are no body forces e.g., gravity that hinders this.

Sol: A dispersion in which the particles are so far apart that they can move independently. In a *stable* sol the repulsive forces are so strong that should particles come near each other by diffusion or due to effects of gravity, they do not combine to form a new particle.

Critical Coagulation Concentration (CCC): Lowest concentration of a certain solute in water (in this case sodium) needed to form a gel.

Chemical erosion: Detachment of smectite particles due to lack of cohesive forces when the ionic strength of water decreases below CCC.

Flocculation: Aggregation of detached particles into a segregated gel at the rim (interface between expanded bentonite and water). It might be transported away by seeping water or form a protective layer against further expansion and erosion (secondary gel).

1.2 State-of-the-art modelling approaches

The model developed by Neretnieks and coworkers (Neretnieks et al. 2009, Liu et al. 2009, Moreno et al. 2010), from now on referred to as KTH model, was the first phenomenological approach to describe bentonite expansion and erosion. It consists in the coupling of a set of three governing equa-

tions corresponding to sodium cation transport, smectite expansion and water flow in a fracture, with special focus on the smectite diffusion equation, which models bentonite expansion due to water uptake as if it were a diffusive process (Neretnieks et al. 2017). The early work by Ahn et al. (1999) and Kanno et al. (2001), as well as Borrelli and Ahn (2008), directly based the diffusivity of smectite on a precomputed correlation for bentonite swelling pressure. The KTH model is based on a mechanistic description of the nanoscale forces driving bentonite motion. In that model, the swelling capacity is expressed as a balance between the repulsive Diffuse Double Layer (DDL) force and the attractive van der Waals force. In turn, these forces show an explicit dependence on the two concentration variables of the model – i.e., sodium cation concentration and smectite volume fraction – for which it can in principle be applied to a wide range of scenarios.

Different versions of the KTH model can be found in the literature: the complete model (Moreno et al. 2010) and a simplified version developed by VTT (Finland), named the BESW model (Schatz et al. 2013). The BESW model consists in a simplification of the former for easing its implementation and convergence in COMSOL, with the diffusion coefficient and the sol viscosity being expressed as fitted correlations in terms of sodium cation and smectite concentrations. This approximation overestimated expansion, as shown by Pont et al. (2020), and erosion (Schatz et al. 2013). Moreover, the first model was extended during the BELBaR project with a semiempirical two-region model for the computation of eroded mass at the rim. The development of this two-region model was motivated by the fact that the original continuous model failed to capture this phenomenon (Neretnieks et al. 2017).

Within the POSKBAR project, alternative approaches to the KTH model were also explored. A novel particle-based method using CFD-DEM (computational fluid dynamics and discrete element models) was developed by Laviña et al. (2018) but led to an excessive computational cost. Soil mechanics models based on the Barcelona Expansive Model were also applied, which failed to converge for very large strains due to the unsuitability of the constitutive model for reproducing large deformations and the boundary conditions considered. In this sense, a new soil mechanics model was presented by Islam et al. (2019) for bentonite sealings of oil and gas wells. It also uses a swelling pressure correlation, but in this case, it is coupled with a plastic constitutive model for unsaturated soils. They furthermore modelled the bentonite-fracture contact shear strength for limiting the expansion into borehole fractures. A similar approach was presented by Börgesson et al. (2018), deriving an analytical expression for the penetration depth of bentonite extrusion. In both cases, it showed a linear dependency with the fracture aperture. However, this behaviour was not observed in the laboratory tests presented by Alonso et al. (2019), which showed similar expansion patterns for apertures ranging from 0.2 to 1 mm in cases considering stagnant low salinity waters. This might be partly due to the swelling pressure decrease in the hole for thicker apertures, as well as by uncertainties related to the presence of air bubbles at the bentonite-water interface, which might affect the rheological properties of the gel. However, it will be shown in Section 6 that these factors alone cannot explain limited expansion in dilute waters below CCC.

In the present report, the scope of the KTH model is extended to include other physical processes, in an attempt to increase the level of understanding of some of the important phenomena behind bentonite expansion and erosion. These processes include fluid non-linearities, viscous effects leading to wall friction, and chemical erosion. Pont et al. (2020) proposed several insights that are further investigated and evaluated in the present work, focusing above all on the fluid behaviour of the smectite-water mixture in environments with low sodium concentration and very low ionic exchange with calcium. Several theoretical and experimental studies were carried out in this area: Moreno et al. (2010) deployed Darcy's law with a single Newtonian fluid model (Adachi et al. 1998) for the most dilute region, whereas Neretnieks and Moreno (2018b) also included the non-linear rheology of non-expanding gel between 3 and 6 wt% under the form of a Herschel-Bulkley model (Pujala 2014). Birgersson et al. (2009) proposed a concept with four different domains including solid, gel (stress-strain relation), semi-fluid (Power law) and fluid (Newtonian). However, a 3D Stokes-based model accounting for continuous interaction through viscous shear between groundwater, sol, and dilute gel above the Newtonian range has not yet developed.

On the other hand, (Neretnieks et al. 2009) argued that wall friction in bentonite extrusion in fractures filled with water below CCC appears only at the outermost region, where segregated non-expansive gel accumulates and exerts shear resistance against the expanding paste behind it (Neretnieks and Moreno 2018b). Unlike Birgersson et al. (2009), it excluded the contribution of the whole contact surface with the expanding paste following the DLVO theory, which claims that the negatively charged

smectite platelets will tend to compensate this structural charge with a surrounding diffuse double layer (DDL) of water, thus preventing load transmission to the wall. In this region, only big electroneutral mineral particles are expected to oppose smectite expansion, either in form of dry friction (Börgesson et al. 2018) or through fracture clogging (Richards 2010). In the present work, this theory has been assumed as valid, excluding the effect of big particles. Despite the generally accurate results obtained in Section 6, a brief discussion including uncertainties and open issues regarding this concept has been included in Section 8.

Chemical erosion of the buffer is, together with unbounded expansion, one of the major concerns in the long-term safety assessment of a KBS-3 repository. It refers to the decomposition of smectite into colloids due to the presence of groundwater with ionic strength below CCC, and the subsequent material loss because of flow drag or gravity. In this sense, SKB (2004) proposed a mass balance approach for estimating the buffer erosion rate assuming an equivalent flow rate (Q_{eq}) and the dilution of calcite, leading to values ranging from 0.0032 to 0.4 kg·yr^{-1} (3 000 to 375 000 years up to loss of integrity damage) depending on the initial calcite concentration. On the other hand, Liu and Neretnieks (2006) revised the previous model assuming real flow rates and replacing calcite by gypsum (0.7 wt%), which is considered the real driver of calcium concentration in the buffer. In this case, buffer performance was expected to deteriorate beyond 11 000 years (Arthur 2011). However, the SR-Can Safety Assessment (SKB 2006) considered only pure-Na montmorillonite, which is also the focus of the present work. Three different hydrogeological models were considered – continuous porous medium (CPM), fully correlated discrete fracture network (DFN) and semi-correlated DFN, being the latter the worst case with 35 % of the deposition holes affected by erosion after 25 000 years (Arthur 2011).

Nowadays, these results are considered rather conservative. In recent years, significant efforts have been devoted to the development of small-scale laboratory tests. A significant resistance to bentonite expansion and erosion was observed in these tests, reproducing the conditions that can lead to an unstable gel. The presence of wall friction and fracture partial clogging due to the formation of secondary gel from flocs formed by the reassembly of detached colloids (Neretnieks and Moreno 2018a) requires an extension of the best-estimate numerical models. At the same time, the erosion rate predicted by the coupled model in Neretnieks et al. (2009) was exceeded in one or two orders of magnitude by the upscaling to repository conditions performed with laboratory tests (Smith et al. 2017). This significant disagreement can be explained by the lack of chemical erosion in the model at that stage. This issue has been later addressed in Neretnieks et al. (2017), who proposed a flocculation sink term in the smectite expansion equation based on a semi-empirical coefficient. In Section 4.4.4, this concept is reformulated from a more mechanistic point of view. However, the subsequent motion of the flocs under gravity or groundwater flow has not been yet included in the model. Instead, it has been assumed that all flocs generated during expansion automatically count as lost mass.

With regards to the effect of sloping fractures on the erosion rate, Birgersson et al. (2009) proposed a model for sedimentation of particles under gravity based on the Mason-Weaver equation (Mason and Weaver 1924) after adjusting a parameter with several experimental tests. In the present work, the effect of gravity has been included in the flow equations as a sort of mechanical erosion. At the current state of the model, the extruded smectite is treated as a continuum. Individual particles or flocs cannot be yet considered as independent entities with their own motion. It is assumed that colloids are detached when gravity-increased shear overcomes the cohesive forces between smectite sheets. In reality, gravity only enhances the transport of chemically eroded colloids away from the rim. The performance of this analogy will be carefully analyzed in Section 6. According to Schatz and Akhanoba (2017), the total erosion rate shows a linear dependence on the fracture aperture for both horizontal and sloping configurations in small-scale tests. This result will be used to validate the model in Section 6 and to detect any deviations caused by fracture clogging.

1.3 Limitations of the KTH model

The KTH model succeeded in reproducing the physics behind bentonite expansion without resorting to empirical approaches. However, in a strict sense, the model is only valid for free swelling, since it does not account for viscous forces due to confinement, for instance wall friction, that would limit the expansion of smectite paste in scenarios below CCC. In these cases, the model led to an overestimation of the expansion (Neretnieks et al. 2017). This disagreement was not only related to the physical

assumptions of the model, but also to the conceptual model behind bentonite expansion. This issue is related with the smectite diffusivity model proposed by Liu et al. (2009), which deals with the equilibrium between high force gradients at the nanoscale, yielding a significant concentration gradient at the expanding front. In cases without fracture flow, the bentonite transport is reduced to a diffusion equation, which will lead to unlimited expansion for as long as this concentration gradient persists. Limiting the expansion of bentonite has previously been studied from different perspectives, including soil mechanics with wall friction (Börgesson et al. 2018), bentonite shear strength (Neretnieks and Moreno 2018b) and particle clogging (Richards 2010), but has not been assessed in the KTH model yet.

From a chemical viewpoint, the KTH model is limited to the effect of the sodium cation concentration on the swelling capacity of the clay. This is of course a huge simplification of all the chemical processes involved in the bentonite-fracture system, for which it can a priori only be applied to sodium homoionised bentonites in sodium chloride solutions. Still, this approach can be considered as a worst-case estimate because commercial bentonites in contact with low salinity waters (i.e., glacial water) will absorb calcium even in cases with very low Ca concentration, which is known for reducing the clay swelling capacity and thus the risk of erosion. This issue has been recently analysed by Neretnieks and Moreno (2021) but will be left out of the scope of the present report.

Another issue with the KTH model is that mechanical erosion due to fracture water flow is significantly underestimated. There might be several reasons behind this disagreement which will be analysed in Section 4, among which the lack of viscous shear stress in Darcy's law, the exclusion of the compacted bentonite pellet from the model domain, and the use of a simplified 2D geometry, may be the key factors. In any case, the KTH model provides a reduced interaction between sol and seeping water as the viscous stresses between the different phases (gel, sol, water) cannot be properly captured with Darcy's model, thus preventing erosion. A two-region model was developed to compensate this deficit and the results were significantly improved (Neretnieks et al. 2017). It consists in the solution of a second transport problem where the advective term coming from the flow equation is replaced by a sink computed from mass balance considerations. This sink in turn depends on an erosion rate that is estimated in a semi-empirical fashion using a previously obtained rim perimeter.

Finally, chemical erosion is the other key factor in the loss of bentonite that has not yet been included in a computational model, although significant efforts have been made at an experimental level for understanding the physical mechanisms behind this phenomenon (Neretnieks et al. 2017, Smith et al. 2017). The disaggregation of the sol during expansion is known to be driven by the chemistry of water and bentonite, but a sudden change in the fluid consistency due to non-linear effects could also explain flocculation from a mechanical point of view. In fact, gravity-driven cases show a higher erosion rate than horizontal test configurations (Neretnieks et al. 2017). This issue will be addressed in Section 4.4.4.

2 Objectives and scope

The final goal of the project is to develop a numerical model that is tested against experimental data and that can be used to predict the expansion and erosion of water saturated bentonite in a repository using transport and water-gel flow equations in fractures. Different mechanistic models have been proposed (e.g., Neretnieks et al. 2017) but significant discrepancies remain between experimental and modelling results due in part to the unexpected relevance of gravity, wall friction, and chemical erosion, in some cases.

At this stage, the present study focuses on the long-term quantification of all buffer mass loss processes under repository conditions: mechanical erosion due to shear stress induced by groundwater flow, chemical erosion due smectite disaggregation into colloids, and sedimentation due to gravity in sloping fractures. To this end, several important features have been implemented in the model. First, a non-linear rheological model that allows a proper representation of the interaction between seeping water and dilute sol (Neretnieks and Moreno 2018b). Secondly, the shear resistance of the non-expansive segregated gel in form of flocculation that appears at the expansion front when the sodium concentration decreases below CCC and the ionic exchange ratio with groundwater calcium is not high enough to bring the gel back to a cohesive state (Arthur 2011). The accumulation of these flocs, despite being a hazardous feature in terms of buffer integrity, might also lead to a certain degree of fracture clogging and protection against further erosion. This accumulation can be associated to a wall friction effect, due to the inherent shear resistance of the material acting against the expansive character of the paste behind it. In fact, limited smectite expansion in stagnant water or low flow rates below CCC for clays without accessory mineral particles has been observed by Schatz et al. (2013) and Alonso et al. (2019).

From a chemical perspective, although the scope is neither to extend the model to the transport of other cations different than sodium nor to the effect of accessory minerals, chemical erosion is also considered in the model. Although it is based on the paste deformation rate during expansion, as proposed by Sato et al. (2004), the model is not directly coupled with the flow equations, as will be shown in Section 4.4.4. The advantage of this assumption is the ability to separate and independently assess the mechanical and chemical erosion modes. Finally, gravity effects in sloping fractures are also analysed, as well as its relevance depending on the fracture aperture.

All these ingredients will provide the total erosion rate, extrusion profiles and expansion evolutions that are tested in Section 6 using experimental data corresponding to small-scale tests. In Section 7, the model is applied to a 3D buffer geometry under realistic repository conditions expected during glacial water intrusion periods. This will constitute a new step towards a best-estimate Performance Assessment of the KBS-3 repository concept.

3 Methodology

The description of bentonite expansion and erosion consists of a coupled multiphysics system, characterized by three governing equations: sodium cation transport, smectite expansion, and flow dynamics. All of them are solved in the computational platform COMSOL Multiphysics version 5.4 (COMSOL 2018) based on the finite element method and a staggered coupling scheme, which solves the three equations sequentially up to convergence in the above-mentioned order.

The sodium concentration of the bentonite porewater is not expected to change over the short time spans of the simulated tests (ranging from 19 to 60 days). In other words, the diffusion of sodium cation to the seeping water will not wash the bentonite out. Here one needs to consider the smectite structural negative charge. According to the Donnan equilibrium model (Birgersson and Karnland 2009), this will prevent the leaching of sodium to a great extent if no other cation is present in the solution. This means, that the small sodium plume in the buffer/pellet vicinity will be rapidly removed by the fracture water flow. Moreover, the effect of other chemical species or accessory minerals on the chemical composition has not been considered, although they might play an important role, especially in closed configurations such as the tests by Alonso et al. (2019). For this reason, only cases with water flow have been considered. However, for long-term scenarios corresponding to realistic buffer configurations, the leaching of salts from the bentonite buffer may not prevent that CCC is reached at the buffer-fracture interface under the effect of glacial meltwaters, leading to a scenario of massive erosion once the initial disaggregation allows the flow to penetrate in the buffer. According to the estimations presented in Pont et al. (2020), this point might be reached after approximately 20k years when assuming Donnan equilibrium between bentonite and water and the fracture transmissivities proposed by SKB (2006, Section 9.2.3, p 212) ($< 10^{-7}$ m^2/s). To simplify the simulations, the sodium transport equation has not been solved in the bentonite buffer domain and a constant concentration of 10 mM has been prescribed on the buffer/pellet outer surface, as in Schatz et al. (2013) for MX-80 bentonite.

In Section 4, all extensions to the KTH model regarding bentonite expansion and erosion are presented. Before proceeding with the validation of the model, presented in Sections 6.2 and 6.3, the yield strain rate parameter of the rheological model (see Section 4.3.2) is calibrated in Section 6.1. Model validation is performed with a series of small-scale experiments covering a wide range of transmissivities and dimensions (Schatz et al. 2013, Alonso et al. 2019 and Appendix D). A total of eight simulations between these three sections, listed in Table 3-1, have been computed.

Finally, the tested model has been applied to a realistic buffer geometry for a long-term simulation under glacial water intrusion conditions. In Section 7, three additional scenarios with different transmissivities and fracture slopes have been simulated (Table 3-2).

Table 3-1. List of small-scale bentonite erosion simulation cases with Na-homoionised MX-80 bentonite analysed in Section 6. Reference [1] Schatz et al. (2013), [2] Alonso et al. (2019), [3] Schatz and Akhanoba (2017), [4] Appendix D.

Case	Test (Ref.)	[Na^+] [mM]	Water flow rate [ml/min]	Fracture aperture [mm]	Channel width [cm]	Initial dry density [kg/m^3]	Duration [h]
1	11[1]	0.03 (DI)	0	1	24	1 591	720
2*	51A[2]	1	0	0.2	17	1 400	720
3	3[1]	2.1	2.56	1	24	1 591	456
4	5[1]	0.03 (DI)	0.38	1	24	1 591	672
5	6[1]	0.685	0.09	1	24	1 591	672
6	2[3]	0.685	0.09	1 (45°)	24	1 591	720
7	2[4]	1	0.0313	0.1 (90°)	17	1 420	1 512
8	5[4]	1	0.057	0.1 (90°)	17	1 100	1 512

* Minerals and salt-free MX-80 clay.

Table 3-2. List of large-scale bentonite erosion simulation cases analysed in Section 7.

Case	Ref.	$[Na^+]$ [mM]	Water velocity [m/s]	Fracture aperture [mm]	Fracture slope (°)	Initial dry density [kg/m^3]	Simulation time [y]	Wall friction term
1	1	1	10^{-5}	1	0	1 591	100	No
2	1	1	10^{-6}	1	0	1 591	100	No
3	*	1	10^{-9}	0.4	45	1 591	10	Yes

[1] Schatz et al. (2013, Appendix C, Table 1, first two rows with transmissivities 1×10^{-7} and 1×10^{-8} m^2/s) for comparison.
* This report, Section 7.3.

4 Description of conceptual model

4.1 Model geometry

4.1.1 Small scale tests

The experimental setups developed by Alonso et al. (2019), Schatz et al. (2013), Schatz and Akhanoba (2017) and Appendix D are shown schematically in Figure 4-1. In all cases, the assembly includes a planar fracture between two plates, which contains a hole for a pellet of compacted bentonite. The only differences between the different setups are the dimensions of the different components, which are summarized in Table 4-1. A full three-dimensional representation of the experiments is considered, without assuming any symmetry plane, in order to account for configurations with flow and slope. Solving the equations in the initial bentonite domain allows a precise calculation of the swelling pressure in the fracture, which might decrease in small-scale tests due to the small size of the sample.

Table 4-1. Main features of the different setups corresponding to the small-scale bentonite erosion simulation cases analysed in Section 6.

Tests (reference)	Fracture size [cm]	Pellet shape	Pellet height [cm]	Pellet outer diameter [cm]	Pellet inner diameter [cm]	Initial dry density [kg·m^{-3}]
Alonso et al. (2019)	17 x 17	cylinder	1	1.9	-	1 400
Schatz et al. (2013)	24 x 24	cylinder	2	2	-	1 591
Schatz and Akhanoba (2017)	24 x 24	cylinder	2	2	-	1 591
Appendix D	17 x 17	Hollow cylinder	1.5	2	0.9	1 420
Appendix D	17 x 17	Hollow cylinder	1.5	2	0.9	1 100

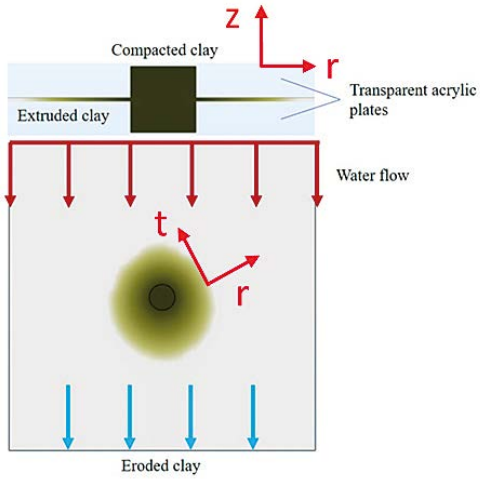

Figure 4-1. *Schematic conceptual model with a planar fracture cutting through a cylindrical bentonite pellet (Neretnieks et al. 2017) showing the radial (r), tangential (t) and vertical (z) directions of the 3D domain.*

4.1.2 Repository conditions

For the long-term buffer integrity evaluation analysed in Section 7, a geometrical setup composed by the reference 3D geometry of the installed KBS-3 buffer (SKB 2011) together with a single horizontal fracture 5.5 m × 8 m (Sena et al. 2010) with two different fracture apertures of 1 and 0.4 mm (Figure 4-2). Solving the smectite transport in the buffer domain allows a better quantification of the mass losses as well as the estimation of the onset of advective transport in the buffer (when dry density = 1 000 kg/m^3).

Although a 45º sloped fracture has been considered in case 3 (see Table 3-2), the setup has not been modified and the effect of gravity has been only included in the flow equations, as if the whole geometry had been rotated.

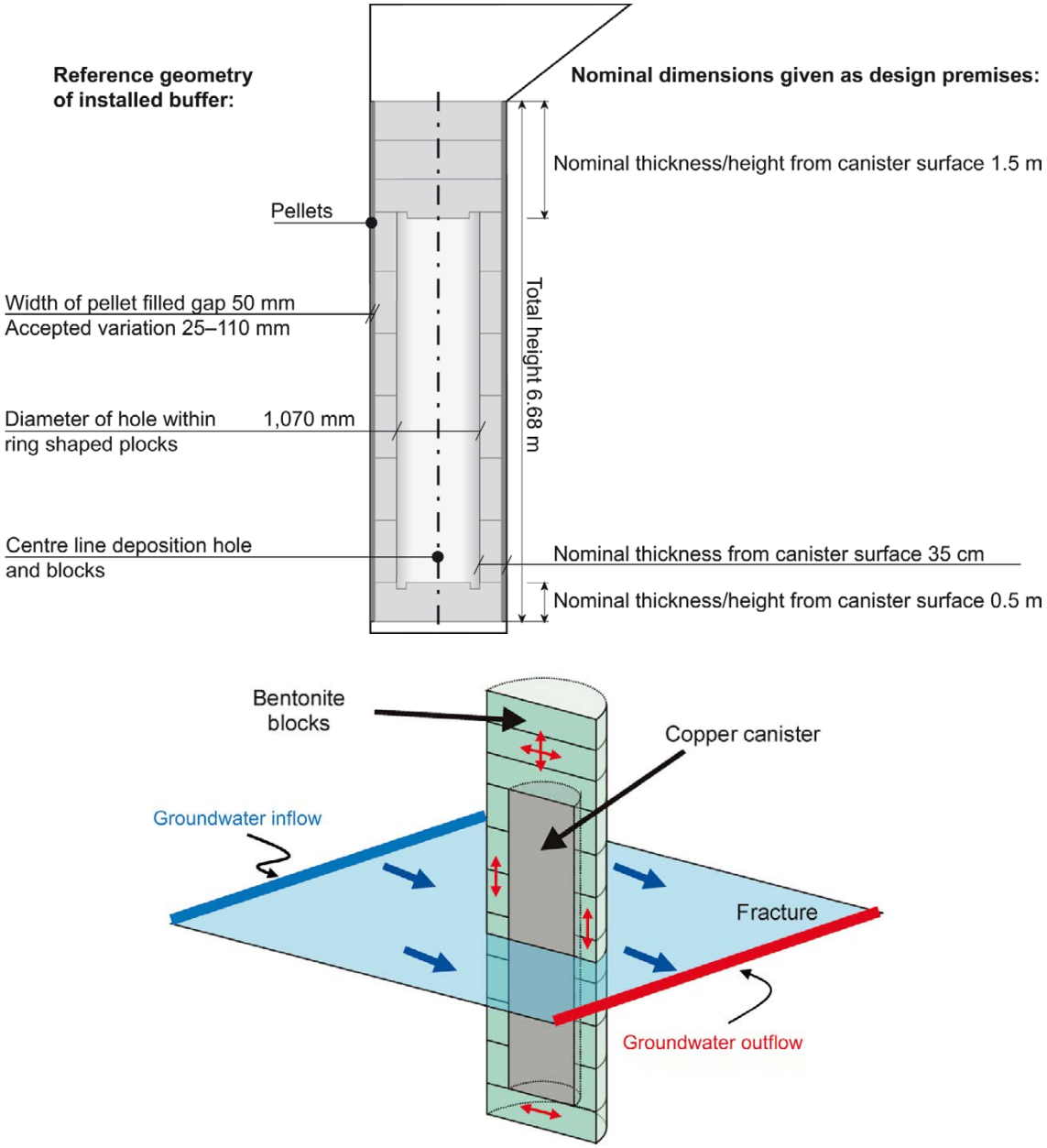

Figure 4-2. *Dimensions of the buffer in the KBS-3 repository (SKB 2011) and schematic representation of a horizontal fracture crossing the bentonite buffer (Sena et al. 2010).*

4.2 General principles

The present modelling study stems from the model for bentonite expansion and erosion proposed by Liu et al. (2009), Moreno et al. (2010) and Neretnieks et al. (2009). In the present work, some modifications and extensions of the model are proposed following two general principles: (1) continuity, including the solution of the smectite expansion equation not only in the fracture domain but also in the compacted clay region, and (2) stronger coupling between the governing equations for physical consistency.

The first principle refers to the necessity of accounting for both buffer degradation and shear velocity at the rim region, for a better assessment of the balance between expansion and erosion. In this sense, an alternative flow model based on the Stokes equations is proposed here to account for viscous flow effects and fluid non-linearities at the dilute outer region.

The second principle aims at reproducing the fundamental physics behind bentonite expansion and erosion, limiting the use of empirical approaches, and striving forward to a physical unification for general use. This implies that the water flow and smectite expansion equations need to be more intimately coupled, for instance, including wall viscous friction in the smectite transport equation. Furthermore, the fit of empirical relations is limited to the flocculation constant (Section 4.4.4) and the yield strain rate of the Herschel-Bulkley model (Section 4.4.2), which depends on the bentonite type and its aging. In both cases, the obtained values in the calibration tests have been applied to all other performed simulations. The use of these empirical relations could be replaced by more mechanistic descriptions of these processes in the future, provided enough experimental data becomes available.

4.3 Fluid mechanics – water flow and non-expansive gel

4.3.1 Stokes equations

The general form for a creeping fluid flow (Stokes flow) is shown in Equation 4-1. The flow model in Moreno et al. (2010) is limited to Darcy's law, which constitutes the most common approach to the calculation of laminar flow with constant viscosity in porous media. With this model, fluid and solid matrix remain as clearly separate phases. However, the studied system does not fulfil this hypothesis because the seeping water progressively changes the rheological properties of the expanding bentonite front within the fracture. This leads to two specificities: on one hand, the appearance of viscous effects related to wall friction, and on the other, the interaction of seeping water with the dilute sol and the segregated gel, which can trigger an erosion process. For these two reasons, shear stress effects need to be considered and therefore a diffusive viscous term (second term in Equation 4-1) is considered, instead of the Darcian term.

In turn, consideration of this term allows accounting for complex rheological phenomena. Equation 4-2 states the relation between shear stress, τ, the effective viscosity, η_{eff}, presented in Section 4.3.2, and the strain rate $\nabla^S \vec{u}$ (∇^S being the symmetric gradient). The strain rate is also referred to as $\dot{\gamma}$, which corresponds to the symmetric velocity gradient tensor.

Although water flow is considered incompressible, the continuity equation (Equation 4-3) allows water storage in the expanding clay in a similar way as in traditional porous media, allowing for weak compressibility effects due to density changes:

$$\rho \partial_t \vec{u} - \nabla \cdot \tau + \nabla p = \vec{0} \qquad \text{Equation 4-1}$$

$$\tau = \eta_{eff} \nabla^S \vec{u} = \eta_{eff} \dot{\gamma} \qquad \text{Equation 4-2}$$

$$\partial_t \rho + \nabla \cdot (\rho \vec{u}) = 0 \qquad \text{Equation 4-3}$$

In these equations, $\rho = \varphi\rho_s + (1 - \varphi)\rho_w$ is the water-bentonite mixture density (kg·m^{-3}), φ is the smectite volume fraction (-), ρ_s and ρ_w are the solid (or grain) and bulk densities (kg·m^{-3}), respectively, η_{eff} is the dynamic effective viscosity (Pa·s), defined in the following section, $\vec{u}$ is the velocity (m·s^{-1}) and p is the pressure (Pa).

As boundary conditions, a no-slip condition (i.e., zero velocity) is prescribed on all model contours except the fracture inlet and outlet, where a water flowrate (Table 3-1) and an open boundary condition are imposed, respectively (Figure 4-1). This leads to the typical parabolic velocity profile observed in laminar flows between two parallel plates. In this sense, no simplifications or analytical solutions have been used and the full set of the Stokes equations (Equations 4-1 to 4-3) was solved at all time steps for adapting to the varying smectite mass distribution in the domain. The flow initial conditions were derived with a stationary solution of the Stokes equations accounting for the described boundary conditions.

Based on general principles listed above, it seems justified to strive towards a flow model for bentonite mechanical erosion that only relies upon physical principles. At this stage, the presence of the rheological model only affects the outermost dilute phase, which may interact with seeping water and move accordingly. Due to the sharp viscosity increase with smectite volume fraction (Neretnieks and Moreno 2018b), denser expanding paste will not move because of the seeping water flow shear force. This slip between phases will be automatically captured by the flow solver as a shear layer. The expansion motion of the denser paste will be reflected in the smectite transport equation as a diffusion flux. The Stokes equations do not rely on permeability models, as the Darcy (Moreno et al. 2010) and Brinkman equations, which might introduce new uncertainties to the calculation of the erosion rate. Instead, this approach, combined with an appropriate rheological model, will describe the interaction between water, dilute sol, and segregated gel in a continuous fashion as a slurry flow, relying only on shear resistance for balancing the pressure gradient caused by the seeping water flow. This approximation to bentonite erosion is expected to prevent both the strong underestimation yielded by the Darcy equation and the need of correction with a two-region model in Neretnieks et al. (2017). The latter assumes a fixed rim concentration, φ_R (-) and solves a second smectite transport problem in this outer region, replacing the convective term coming from the flow equations for a sink term coupled with a mass balance equation. The erosion rate, N_{er} (kg·s^{-1}), is modelled with the following expression:

$$N_{er} = \rho_s \delta \varphi_R \frac{4}{\sqrt{\pi}} \sqrt{D_R \pi r_R u_0}, \qquad \text{Equation 4-4}$$

where D_R is the smectite diffusion coefficient at the rim concentration (m^2·s^{-1}), r_R the expansion radius (m), u_0 is the approaching water velocity (m·s^{-1}), ρ_s is the smectite particle density (kg·m^{-3}), and δ is the fracture aperture (m). This method requires tracking the rim region at $r_R(t)$ and defining an appropriate φ_R for each scenario. In some cases, it overestimates erosion (Neretnieks et al. 2017), and in others, such as gravity driven tests, it fails in capturing erosion above rim concentration.

4.3.2 Herschel-Bulkley rheological model

One of the main challenges is to capture with a single model the behaviour of the solid and fluid phases simultaneously. Whereas the behaviour of compacted bentonite has been traditionally studied from the soil mechanics perspective (e.g., Gens 2010), dilute gel and sol have been modelled as non-Newtonian fluids (Neretnieks and Moreno 2018b). If the problem is restricted to a solid extrusion (e.g., Börgesson et al. 2018) and a balance is derived between swelling pressure and the static friction stress, the expansion distance can be shown to be directly proportional to the fracture aperture, δ (m). This result disagrees with the experimental tests performed by Alonso et al. (2019), which show that the final expansion does not increase significantly in the range δ = 0.2–1.0 mm. This non-linearity can be partly attributed to the decrease of swelling pressure in the hole, which becomes more significant with increasing fracture apertures. The presence of gas bubbles, which has been often observed in small-scale tests, can also introduce uncertainties in the prediction of bentonite extrusion. However, neither of these factors can explain the limited expansion observed in tests performed with low-salinity water below CCC (Schatz et al. 2013, Schatz and Akhanoba 2017, Alonso et al. 2019).

One way to remedy this is to consider the viscous shear stresses (τ, in Pa) of the fluid phase in Equation 4-1 including the nonlinear effects observed in the typical concentration range of the dilute segregated gel ($0.01 < \varphi < 0.02$) fitted by Pujala (2014) with a Herschel-Bulkley model for non-Newtonian fluids:

$$\tau = \tau_0 + k_{HB} |\dot{\gamma}|^n, \qquad \text{Equation 4-5a}$$

$$\tau_0 = 0.2 \left(100 \frac{\varphi \rho_s}{\rho}\right)^3 \qquad \text{Equation 4-5b}$$

where τ_0 (Pa) is the yield (or mobilization) shear stress, which is the minimum stress needed for mobilizing the smectite paste, $\dot{\gamma}$ is the strain rate (s^{-1}) and k_{HB} (Pa·s^n) and n (-) are the two parameters of the model, which are defined as $n = 0.45$ and

$$k_{HB} = 130\frac{\varphi\rho_s}{\rho} - 2.3, \qquad \text{Equation 4-6}$$

where φ is the smectite volume fraction (-), ρ_s is the solid or grain density (kg·m^{-3}), and ρ is the bulk density (kg·m^{-3}). Note that Equation 4-5a will replace its generic form presented in Equation 4-2.

Non-linear effects have already been observed in very dilute suspensions (Pujala 2014), for which this regression of the Herschel-Bulkley model is proposed for the whole domain except for $\varphi < 0.01$, where the Newtonian fluid model proposed by Adachi et al. (1998) will apply (see Appendix A):

$$\eta_{eff} = \eta_0 = \tau_0|\dot{\gamma}_0|^{-1} + k_{HB}|\dot{\gamma}_0|^{n-1} \text{ if } |\dot{\gamma}| \leq \dot{\gamma}_0 \qquad \text{Equation 4-7a}$$

$$\eta_{eff} = \tau_0|\dot{\gamma}|^{-1} + k_{HB}|\dot{\gamma}|^{n-1} \text{ if } |\dot{\gamma}| > \dot{\gamma}_0 \qquad \text{Equation 4-7b}$$

This formulation is thought to be suitable to represent the phenomenology behind the motion and erosion of smectite gel and sol, which is driven by large viscosity gradients leading to different consistencies in terms of shear resistance. These different behaviours are captured in a continuous fashion by the viscous term (second term in Equation 4-1). Thus, the Stokes model can be solved in the whole bentonite-water domain. Additionally, it will provide a proper background for the viscous shear resistance to expansion exerted by the segregated gel that will accumulate beyond the expanding front in cases below CCC with insufficient calcium absorption. Note that this approach to wall friction is equivalent to that proposed by Neretnieks et al. (2009) and Neretnieks and Moreno (2018b) and may provide a more realistic interpretation of the experimental results obtained by Schatz et al. (2013) and Alonso et al. (2019) than the solid friction model (Börgesson et al. 2018). The latter could hypothetically be restricted to the effect of accessory particles. In Section 4.4.2 a detailed development of the wall friction model is presented.

4.4 Smectite transport

4.4.1 Derivation of a wall friction term within the DLVO model

The diffusion-like transport of smectite due to swelling in low salinity water is described by Liu et al. (2009), which derives the diffusion coefficient as the quotient of a diffusivity function, χ (J), and a friction factor, f (kg·s^{-1}). The former expresses a force balance at the nanoscale between DDL (diffuse double layer) repulsive and van der Waals attractive forces (Equation 4-8). The friction factor acts as a penalty function due to frictional forces between water and smectite sheets (see Appendix A). This model is of key importance for providing a physically based smectite expansion equation in terms of its volume fraction (φ). It is also essential to calculate the key parameters of the flow equations – density, viscosity, and swelling pressure – and ensuring a proper coupling between both physics.

$$\partial_t\varphi + \vec{u}\cdot\nabla\varphi - \nabla\cdot\left(\frac{\chi}{f}\nabla\varphi\right) = 0 \qquad \text{Equation 4-8}$$

In the present study, the previous coupling is preserved, but in line with the presented general principles, the smectite expansion equation covers the whole domain in a continuous fashion. It is noted that the smectite volume fraction at the interior of the bentonite pellet could non-negligibly decrease with time, even for short test durations. Moreover, a convective term is included in the smectite transport equation to establish a counterforce against diffusion (which drives the expansion) and the effect of viscous shear (which restricts the expansion). In cases with water flow, this expansion limitation might be provided by erosion, but in stagnant cases the KTH model does not provide a counteracting force that limits free swelling, which will continue for as long as the diffusivity function is larger than zero and there is a non-zero smectite concentration gradient at the rim (Neretnieks et al. 2017).

Regarding boundary conditions, closed walls (i.e., zero concentration gradient in the normal direction) are prescribed on all model contours except the fracture inlet and outlet, where an infinitesimal smectite volume fraction (non-zero value) and an open boundary condition are imposed, respectively. Initially,

the fracture domain is assigned the same infinitesimal smectite concentration (clean water), whereas the initial bentonite pellet domain (Figure 4-1) is given the volume fraction corresponding to the bentonite dry density values in Table 3-1.

4.4.2 Shear resistance due to non-expansive gel below CCC

The fluid mechanics model in Section 4.3 is suitable for describing water flow in a fracture where expansion and erosion would tend to balance each other until reaching a pseudo-steady state. However, when considering the case of smectite expansion in contact with a very slow flow or stagnant low salinity groundwater (below CCC), mechanical erosion due to flow is not a relevant issue anymore (Smith et al. 2017). In that case, the main concern regarding the long-term stability of the bentonite buffer is whether the smectite gel will expand indefinitely or whether it could stop by some sort of resistance to motion. Experimental results show both possibilities: on one hand, Alonso et al. (2019) found a bounded expansion with $[Na^+]$ = 1 mM, whereas Schatz et al. (2013) did not observe steady state conditions for 30 days when using deionized water. However, it should be noted that the salinity of the solution in the fracture increased above the CCC during the experiments of Alonso et al. (2019). The potential role of sedimentation and clogging of relatively large accessory mineral particles is out of the scope of this study. Instead, focus is made on the role of wall friction in the radial direction as a result of shear resistance due to flocculation at the rim during expansion. Shear stress in the tangential direction due to the presence of flow is not accounted for in the smectite transport equation as it is already captured by the Stokes equations.

The quantification of the resistance against 'diffusive expansion' is a key aspect for a more realistic estimation of the total extruded bentonite mass over the long term (100 k or 1 M years). At this point, it must be noted that the extension of the KTH model will not focus on the diffusion coefficient proposed by Liu et al. (2009), which has proved to accurately describe the physics of smectite expansion (Section 6.1). Instead, an additional term is proposed in the smectite transport equation to account for wall friction effects, which in some cases may compensate expansion. This wall friction model is not in contradiction with the bentonite expansion concept proposed by Neretnieks et al. (2009), which assumes that no net movement of the clay-water mixture takes place unless there is a hydraulic gradient, nor with the repulsion between smectite sheets and walls due to the presence of DDL forces presented by Liu et al. (2009). The concept behind the present wall friction model is presented by Neretnieks and Moreno (2018b), who analyzed how the segregated gel flocs that accumulate at the rim can exert a relevant shear resistance in cases where the salinity at the water-bentonite interface decreases below CCC. This effect can be easily captured in the flow equations by an adequate rheological model. However, the smectite transport equation is not affected unless a term accounting for the shear resistance of this gel is included. For this reason, its application has been restricted to cases with salinity below CCC. This phenomenology has then little to do with the hydraulic gradient or the net mass transport in the fracture but is related to the capacity of the segregated gel to block further clay expansion.

According to Liu et al. (2009), the force balance behind smectite transport can be written as follows (neglecting advective flow):

$$\vec{F}_\eta = -\vec{F}_s - \frac{\chi}{\varphi}\frac{\partial \varphi}{\partial \vec{x}}, \qquad \text{Equation 4-9}$$

where $\vec{F}_\eta$ refers to the frictional force between solid and liquid phases, $\vec{F}_s$ to the gravity and buoyancy forces and φ is the smectite volume fraction. The frictional force $\vec{F}_\eta$ can be expressed in terms of the expansion velocity and the friction factor as $\vec{F}_\eta = f\vec{v}$. In this way, a flux of smectite can be defined as $\vec{J} = \varphi\vec{v}$, which after some algebra leads to the following equation (Liu et al. 2009):

$$\vec{J} = -\frac{\vec{F}_s\varphi}{f} - \frac{\chi}{f}\frac{\partial \varphi}{\partial \vec{x}} \qquad \text{Equation 4-10}$$

Mass conservation then reads:

$$\partial_t \varphi = -\nabla \cdot \vec{J} \qquad \text{Equation 4-11}$$

At this point, we redefine the frictional force as $\vec{F}_\eta = f(\vec{v} - \vec{w})$, where $\vec{w}$ is a wall friction velocity that opposes resistance to the free expansion velocity $\vec{v}$, reading:

$$\vec{J} = \vec{w}\varphi - \frac{\vec{F}_s\varphi}{f} - \frac{\chi}{f}\frac{\partial \varphi}{\partial \vec{x}} \qquad \text{Equation 4-12}$$

After imposing mass conservation and neglecting for the moment the gravity and buoyancy forces, $\vec{F}_s$, the smectite transport equation with wall friction can be written as:

$$\partial_t \varphi = -\nabla \cdot (\vec{w}\varphi) + \nabla \cdot \left(\frac{\chi}{f}\nabla\varphi\right) \qquad \text{Equation 4-13}$$

The friction force is implicitly included in the wall friction velocity and appears as a conservative advective term in Equation 4-13 that can be directly implemented in the numerical model. However, $\vec{w}$ still needs to be defined. In fact, it is a virtual velocity that quantifies the resistance to expansion at each point of the domain. For consistency with the fluid mechanics model for a laminar viscous flow (Equations 4-1 and 4-3), $\vec{w}$ can be defined as the average velocity of a viscous laminar flow between two parallel plates, as if wall friction, τ_{fric}(Pa), was the driving traction:

$$\vec{w} = \frac{\tau_{fric}\delta}{4\eta_{eff}} \qquad \text{Equation 4-14}$$

where δ (m) is the fracture aperture and η_{eff} is the effective viscosity given in Equation 4-7. At this point, one needs to define τ_{fric}, which represents the shear resistance exerted by the segregated gel at the expanding bentonite-water interface due to the confinement in the fracture. Although the swelling pressure of the paste behind will always overcome the yield stress of this dilute gel (τ_0 in Equation 4-5), the surface integral of the shear stress after mobilization, now on τ_1, will increase with the expansion radius as the gel accumulates. At some point, it may lead to a limitation of the expansion as observed in several sodium-based small-scale tests below CCC. On the other hand, the strain rate at this region is expected to be several orders of magnitude lower than the typical values of $\dot{\gamma}_0$, which depends on the clay type and its aging, and will be calibrated in Section 6.1.

This should not be confused with the behaviour of the expanding paste, which expands by diffusion while water is suctioned in the opposite direction. Although the motion of the segregated gel at the rim might be driven by swelling pressure overcoming $\dot{\gamma}_0$ at an initial stage of the expansion, the deformation rate will soon slow down until an equilibrium is reached. For this reason, a quasistatic approximation is assumed for both τ_1 and η_{eff}, obtaining the following expression for the wall friction term:

$$\vec{w} = \frac{\tau_1\,\delta}{4\eta_{eff}} = \frac{k_{HB}|\dot{\gamma}_0|^n\,\delta}{4(\tau_0|\dot{\gamma}_0|^{-1}+k_{HB}|\dot{\gamma}_0|^{n-1})} \qquad \text{Equation 4-15}$$

In turn, this approximation will allow using the wall friction model in cases without flow, where the Stokes equations are not solved, since the real strain rate $\dot{\gamma}$ is not necessary anymore as it does not reach the mobilization threshold $\dot{\gamma}_0$ when wall friction is capable of forcing an equilibrium with the expansion force. The term is restricted to the validity range of the Herschel-Bulkley regression presented in Section 4.3.2 ($\varphi \geq 0.01$). Bearing in mind that viscosity is in the denominator, the friction velocity will be more relevant in the lightest phases, for instance the segregated gel, as suggested in Neretnieks and Moreno (2018b). As pointed by Neretnieks and Moreno (2018b), gel viscosity is highly dependent on salinity. However, the presented Herschel-Bulkley rheological mode, is only valid for sodium concentrations from 0 to 5–10 mM. Since $\vec{w}$ depends on η_{eff}^{-1}, the application of the wall friction term must also be restricted to the same salinity range. This is consistent with the range where flocculation and the subsequent shear resistance are prone to appear (Section 4.4.4).

As will be demonstrated in Section 6, wall friction and its scaling with δ presented in the following section yields a satisfactory performance for a wide range of scenarios. However, it significantly overestimates the expansion observed in test 51A (stagnant water in a 0.2 mm fracture and MX-80 without salts and minerals) of Alonso et al. (2019). This result opens an important discussion around the presence of alternative wall friction sources. At this point, one needs to remind that the rheological model has not been validated beyond $\varphi = 0.02$, since it has only been applied to the typical concentration range of a dilute segregated gel. However, it is not yet clear how the denser expanding paste might intervene in terms of wall friction when no accessory minerals are present.

Since this disagreement has not been observed for a similar test with $\delta = 1$ mm, one could also resort to surface tension effects. This force might be large enough to play an important role in the force balance at the expansion front. In fact, it is considered one of the driving forces in microfluidics, where pressure ranges and gravitational forces tend to be negligible with decreasing δ (Vowell 2009, Convery and Gadegaard 2019). See Appendix B for more information on this topic.

An alternative version to this model is currently being developed for separating the expansive phase from the segregated one at the rim. This, in turn, is expected to provide a significant boost of the computational performance (see Appendix C for more details).

4.4.3 Fracture aperture scaling of the wall friction term

It should be noted that the term δ in Equation 4-14 penalizes the expansion for wider apertures, which a priori is not physically sound. However, it is reasonable to consider that the relevance of the viscous layer (δ_{VL}) size also decreases with δ, bearing in mind that in a dimensional sense, it only depends on the distance x from the bentonite source as shown in Equation 4-16.

$$\delta_{VL} = 5.0\sqrt{\frac{x\eta_{eff}}{\rho u_{exp}}} \qquad \text{Equation 4-16}$$

The expansion velocity, u_{exp}, will be similar in all cases, since in a creeping flow it is proportional to the pressure gradient between the hole and the fracture, which in turn is tightly related to the smectite concentration gradient. It will be similar in all cases unless the bentonite buffer is significantly emptied, for example in thicker fractures. This would only happen in case of unlimited expansion or at an advanced degradation stage due to erosion. Therefore, the integral of τ_1 on the fracture section will have to be readjusted to scale the real relevance of the shear stress (see Equation 4-17). Otherwise, the value of the average friction velocity $\vec{w}$ would be unrealistic.

$$\tau_1(\delta_1) = \tau_1(\delta_0) \cdot \left(\frac{\delta_0}{\delta_1}\right) \qquad \text{Equation 4-17}$$

In the present case, $\delta_0 - 1$ mm, which corresponds to the fracture aperture that has been used for the calibration of the wall friction term (see Section 6.1), whereas δ_1 refers to any other aperture within the relevant range.

4.4.4 Flocculation model

Mass losses due to chemical erosion are also of major concern in the long-term safety assessment of a bentonite buffer in the KBS-3 concept. In small-scale experiments, it has been observed that flocculation appears at an early stage of expansion and is only coupled to the chemical composition of the bentonite-water interface. Certainly, flow rate, fracture aperture and gravity will play an important role in the fate of these flocs, but their generation is assumed to be independent of these three factors. For this reason, the implementation of a flocculation rate in the model has not been coupled with the mechanical erosion driven by the flow equations. In this first stage towards the quantification of chemical erosion, a sink term in the smectite expansion equation has been implemented (Equation 4-18). This term assumes that the flocs disappear from the system once they have been formed (Neretnieks et al. 2017). This might be quite accurate in wide fractures (~1 mm), but in narrower ones the seeping water flow might not suffice to drag the flocs downstream. Since fracture clogging is not part of the scope of the present work, this phenomenon will not be considered in the model.

$$\partial_t\varphi + \vec{u}\cdot\nabla\varphi + \nabla\cdot(\vec{w}\varphi) - \nabla\cdot\left(\frac{\chi}{f}\nabla\varphi\right) + R_{floc}\varphi = 0 \qquad \text{Equation 4-18}$$

The coefficient R_{floc} of the flocculation sink term is modelled according to Sato et al. (2004), who proposed a linear dependency on the strain rate of the smectite gel. One could think about using the strain rate computed in the flow equations, but that is the one which triggers mechanical erosion and has nothing to do with the differential deformation of the gel during expansion ($\dot{\gamma}_{exp}$). As stated in Section 4.3.1, the motion of gel cannot be captured by the Stokes equations due to its high viscosity when ($\varphi > 0.01$), unless the fracture flow is way above the standards (3.35×10^{-4} m/yr according to Sena et al. 2010). For this reason, the gel deformation rate (non-symmetric velocity gradient) that is expected to lead to flocculation is extracted from the diffusive flux in Equation 4-18, which can be understood as the smectite expansion velocity. Then, R_{floc} can be formulated as follows:

$$R_{floc} = C\cdot\dot{\gamma}_{exp} = \frac{C}{2}\cdot\left[\partial_y\left(\frac{\chi}{f}\partial_x\varphi\right) + \partial_x\left(\frac{\chi}{f}\partial_y\varphi\right)\right] \qquad \text{Equation 4-19}$$

The sink term is applied to gel phases between $\varphi - 0.001$ and $\varphi - 0.02$, which according to Neretnieks and Moreno (2018b) are more prone to decompose in flocs. Despite the mechanistic approach in Equation 4-19, water composition is the real driver of chemical erosion and flocculation. In this sense, Figure 4-3 shows how R_{floc} will become more relevant with decreasing sodium concentration. The diffusivity gradient in the relevant smectite volume fraction range is more than three orders of magnitude larger for a sodium concentration of 0.1 mM than for 10 mM. This is totally consistent with the experimental observations, which restrict flocculation to sodium concentrations well below 10 mM.

Finally, the constant C in Equation 4-19 has been calibrated in case 5, Section 6.3, using the experimental expansion evolution. After setting $C = 50$ and fitting this curve, the average erosion rate has been perfectly adjusted. Then, this value has been used in all other cases with flocculation in Sections 6.3 and 7.

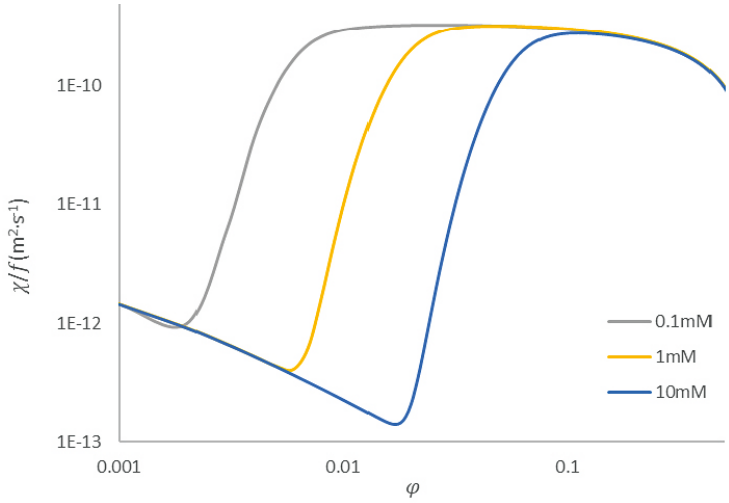

Figure 4-3. *Smectite diffusivity versus smectite volume fraction for three different sodium concentrations according to Liu et al. (2009).*

5 Numerical models setup

5.1 Coupling strategy

The conceptual model described in Section 4 is implemented as a three-dimensional (3D) coupled model (Figure 4-1) using COMSOL Multiphysics (COMSOL 2018). This includes two transport equations, one for Na^+ and the other for smectite, as well as the Stokes equations, which are solved in a staggered fashion (Figure 5-1). At each time step, the depicted information flow is carried out by the solver in an iterative fashion until an automatically calculated tolerance is reached. The Stokes equations provide the advective flow velocities for the two transport equations, whereas the Herschel-Bulkley (H-B) model provides the effective viscosity needed for the wall friction term included in the smectite expansion equation. The smectite volume fraction (φ) is needed for the smectite and sodium diffusion coefficients, and for the fluid viscosity in the Newtonian range, for which the sodium concentration is also required.

However, this tight coupling between all three governing equations still allows a separate assessment of the three different erosion modes considered in the model: flow erosion, chemical erosion, and sedimentation due to gravity. They have been modelled separately and their individual effects on the total erosion rate can be easily quantified. However, this will not be yet consistent with the real physics behind bentonite erosion. The main reason is that small particles and flocs cannot yet be tracked after detachment.

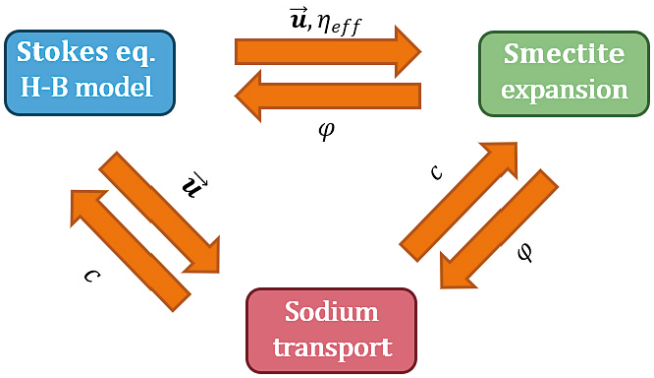

Figure 5-1. *Schematic representation of the coupling scheme considered in this study.*

5.2 Small scale tests

As shown in Section 4.1, the modelled geometry is an artificial fracture with an aperture varying from 0.1 to 1 mm and a bentonite pellet swollen in the hole cut by the fracture (Figure 4-1). Although the two transport equations and the laminar flow problem do not require a fine spatial discretization of the domain, the geometrical setup and the high initial concentration gradients demand an accurate refinement on the external boundary of the pellet and on the two fracture walls (see Figure 5-2). In the first case, the discretization of the perimeter (of the cylindrical bentonite pellet) has been refined to minimize mass losses during the initial transient, whereas the perpendicular direction has been divided in 7 elements for capturing the parabolic velocity profile in the cases with flow. A proper description of the mass transfer between hole and fracture will provide an accurate quantification of the expansion. This, in turn, will have a significant impact on the calculated erosion rate. Although all relevant phenomena in terms of erosion take place at the outer rim, a complete modelling of the hole and the innermost region of the fracture will allow a proper description of the changing boundary conditions for the rim. Elsewhere in the fracture plane, the element size has been set to 3 mm, leading to a mesh with a total number of 105 k linear finite elements for 1 mm fracture apertures. In narrower configurations the pellet-fracture interface has been further refined to provide an accurate resolution, increasing the mesh size up to 200 k elements. The geometries corresponding to the tests in Appendix D have not introduced relevant changes in the final mesh size.

The analysed period ranges from 19 to 60 days depending on the simulated test. Temporal discretization is based on the adaptive time stepping of COMSOL according to local error estimators, as well as the integration scheme, which can switch between BDF1 and BDF2 (BDF = Backward Differentiation Formula).

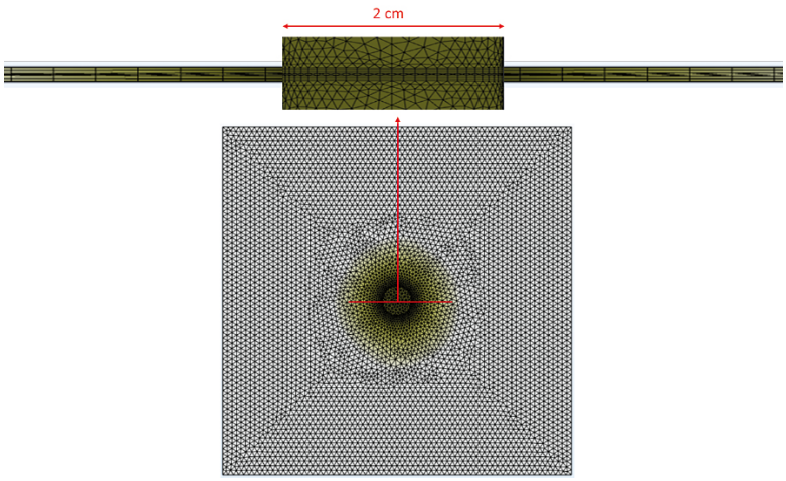

Figure 5-2. *Finite element mesh used in the simulations in Section 6 showing the refinement around the clay pellet (a) and in the fracture (b).*

5.3 Repository conditions

The geometrical setup presented in Section 4.1.2 has been implemented and discretized in COMSOL. As can be observed in Figure 5-3, two planar symmetries have been considered to reduce the size of the computational model: the fracture midplane and the buffer vertical midplane.

All scenarios have been simulated with the same finite element mesh: 150 k linear elements with specific refinement in the fracture (3 hexahedral elements in the half fracture aperture) and on the bentonite – water interface with 7 mm elements. The buffer has been discretized with 0.1 m tetrahedral elements.

The first two cases in Section 7 have been simulated up to 100 years. For computational cost reasons, the case accounting for wall friction (see Table 3-2), which makes solver convergence significantly more difficult due to its advective character, have been limited to 10 years, after checking that both expansion and erosion rate have reached steady state. Then, the calculated evolution has been extrapolated in all cases up to the critical dry density (1 000 $kg \cdot m^{-3}$), beyond which advective flow is expected to intrude the bentonite buffer. At this point, according to Smith et al. (2017), significant vertical gradients may appear as relocation of material inside the buffer is not instantaneous, above all under high erosion rates or low initial dry densities. These voids can of course increase the local damage after the onset of intrusion.

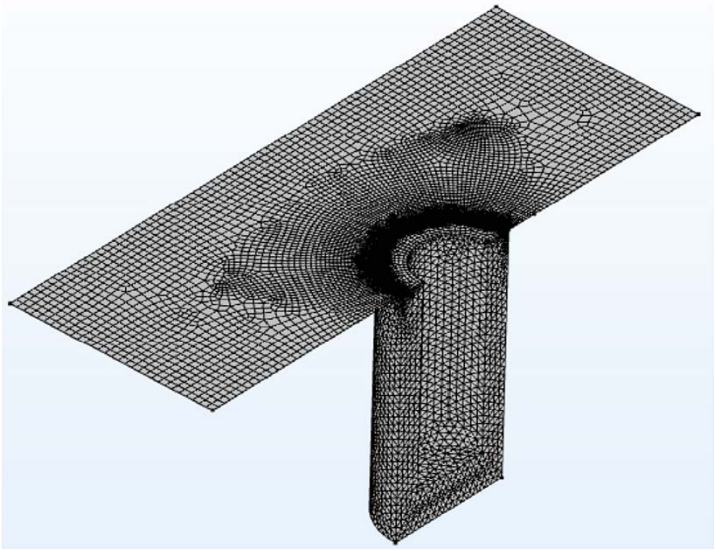

Figure 5-3. *Finite element mesh with buffer-fracture interface refinement.*

5.4 Numerical issues

The development process towards a robust numerical model has required to overcome several numerical issues. The coupling between all the involved physics, despite being the most complex one, has been solved at a conceptual level. The three different erosion modes (flow, chemical and gravity) have been implemented separately. This might be rather conservative in case of low flow rates and narrow fractures, where the flocs can remain near the bentonite-water interface but reflects the independent origin of the three erosion modes. This has allowed simplifying the flow equations in the expanding paste region because no swelling motion has been considered. Instead, this motion, which is relevant indeed for the calculation of the flocculation rate, has been extracted from the smectite transport equation as shown in Section 4.4.4.

During the development and testing phases, two numerical issues have appeared. In first place, a significant mass growth (conservation of mass not fulfilled) has been observed in the cases without flow when applying the wall friction term. Although this term is conservative, a small instability appeared at the expanding front, which led to an unexpected 10 % mass overshoot in a 30 h test. This issue has been solved with the application of isotropic numerical diffusion restricted to the outermost dilute phases, where the instability appeared.

In second place, the inclusion of gravity force in sloping fractures has led to solver convergence issues due to the sharp velocity gradients induced by the free fall of the lightest and less viscous phases. This phenomenon has been observed in 1 mm fractures but not in 0.1 mm apertures, where the viscous layer is much more effective in damping the sedimentation. For this reason, gravity force has been limited to $\varphi > 0.012$ in the first case, which drastically improves convergence while assuming a small error in the total eroded mass.

6 Results – validation of the model

In this section, all calculated tests correspond to the geometrical setup shown in Section 4.1.1. A wide range of flow regimes and fracture configurations are simulated to test all the extensions of the model presented in Section 4.

6.1 Model calibration

As stated in Section 4, the proposed model is mainly based on mechanistic principles and intends to be applied to a wide range of scenarios. However, the yield strain rate of smectite gel ($\dot{\gamma}_0$), a relevant parameter for both rheological and wall friction models, needs to be defined beforehand. Since it depends on the bentonite type, the undergone treatment, and the aging, the only way to establish a value for this parameter at this point consists in adjusting an experimental expansion curve of a test with stagnant water. In this way, erosion does not disturb the calibration of this parameter.

For this purpose, test 11 of Schatz et al. (2013) with sodium homoionised MX-80 clay, corresponding to case 1 in Table 3-1, has been selected. In that same reference, a parametrization for the Kozeny constant $k_0\tau^2$ in the internal friction term f (Equation 4-8 and Equation A-4) of the smectite diffusivity model developed by Liu et al. (2009) is presented. A value of 5 is prescribed in all cases except in those with stagnant water, where $k_0\tau^2 = 13$ is used instead, which can be understood as an empirical approach. This last value was obtained by Liu (2010) for Na bentonites after fitting several permeability tests. However, its application poses two issues when applied to the present case: no experimental data with sodium Wyoming bentonite (MX-80) for $\varphi < 0.16$ was available (the most expansive phases were not covered by the proposed correlation), and for Wy70 bentonite $k_0\tau^2$ tended to 5 when φ tended to 0. Moreover, according to Liu (2010), the sensitivity of the expansivity with respect to the Kozeny constant was significant. For these reasons, the widely used $k_0\tau^2 = 5$ was also adopted in the current model.

In Figure 6-1 the experimental expansion curve is shown together with the numerical results from Neretnieks et al. (2017) and the curves obtained with the current implementation in Comsol Multiphysics for both $k_0\tau^2 = 5$ and $k_0\tau^2 = 13$. It can be clearly observed how the latter manages to adjust the experimental results properly, whereas only small differences appear when compared to that from Neretnieks et al. (2017), mostly attributable to the numerical scheme used in the present study and the extension of the model domain to include the pellet. However, the curve corresponding to $k_0\tau^2 = 5$ highly overestimates expansion. This deviation could suggest that the smectite expansion model should be adapted to the flow regime, as proposed in Schatz et al. (2013). Instead, this apparent flaw has been used to calibrate the wall friction term (Section 4.4.2), bearing in mind that gel segregation at the rim will be significant in a case with deionised water.

Case 1 has been then recomputed with $k_0\tau^2 = 5$ and the wall friction term, leading to a proper adjustment of the experimental curve when $\dot{\gamma}_0 = 0.045\ s^{-1}$ (see Figure 6-1). This value for $\dot{\gamma}_0$ has been deployed in all the cases listed in Table 3-1 and Table 3-2, showing a proper representation of the experimental results in a wide range of scenarios. With this parameterization, a physically consistent model for general use is obtained. Once the outer size of the smectite extruded disc has been reproduced, the solution in the whole region has been validated with the experimental extrusion profile integrated over three extrusion rings (Figure 6-2). According to Schatz et al. (2013), an unexpected mass accumulation at the innermost region was observed, which led to a higher dry density than in the pellet itself. This could explain, at least in part, the disagreement observed in the first 10 mm.

Regarding flocculation, it will be first included in Section 6.3. Although in the present case flocculation is expected to appear, it does not affect the extrusion distance since no flow is dragging the flocs downstream.

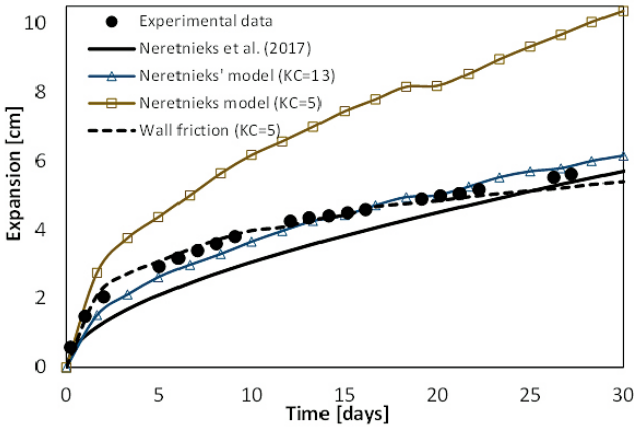

Figure 6-1. *Time evolution of bentonite expansion (in cm) during 30 days in case 1. KC refers to Kozeny's constant.*

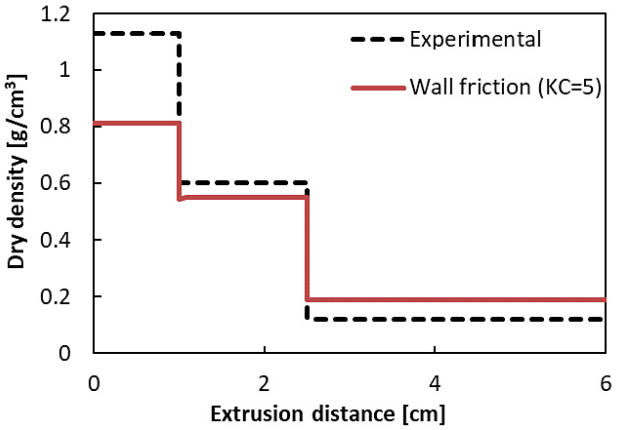

Figure 6-2. *Final smectite extruded density profile after 30 days corresponding to case 1, in terms of bentonite dry density (g/cm^3). The zero value in the x-axis corresponds to the bentonite pellet surface.*

The model has also been applied to a similar case in a 0.2 mm fracture (case 2 in Table 3-1), corresponding to test 51A in Alonso et al. (2019). In this test, purified MX-80 bentonite (i.e., with no salts or accessory minerals) was used. Thus, the uncertainties regarding the chemical composition of the stagnant fracture water are not significant in this case. In fact, a very small change with respect to the original sodium concentration (1 mM) has been measured at the end of the experiment. The importance of this test lays on the uncertainties that arise from the calculated results. It is the only case, as will be shown in Section 6.2 and Section 6.3, where the wall friction model calibrated with the previous test does not reproduce the experimental expansion evolution (Figure 6-3). Several factors, such as the applicability of the presented wall friction concept in narrower fractures, might explain this disagreement. This is briefly discussed in Section 8. One must also consider that the tested bentonite might have slightly different properties than the one used in case 1, for which its yield strain rate $\dot{\gamma}_0$ might not be exactly the same. Although both tests were carried out with sodium montmorillonite, the undergone treatments and the aging might also differ from one case to the other. For this reason, case 2 has been calculated again with $\dot{\gamma}_0 = 0.1$ s^{-1}, leading to a better adjustment of the experimental curve. However, this calibration has not been validated with further tests because test 51A is the only one with purified MX-80 in Alonso et al. (2019). Moreover, the sensitivity of expansion respect to $\dot{\gamma}_0$ shows the necessity of further experimental research in rheological properties of smectite gel.

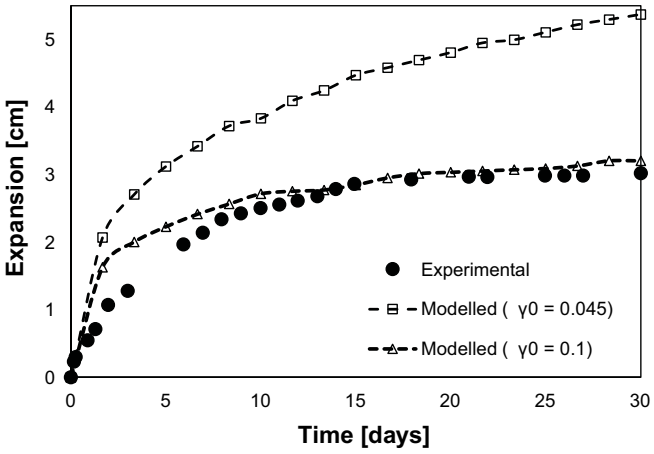

Figure 6-3. *Time evolution of bentonite expansion (in cm) during 30 days in case 2.*

6.2 Quantification of bentonite mass losses due to mechanical erosion

With the calibration of the wall friction term in Section 6.1, the rheological model is fully defined. Therefore, the first feature to be validated is the behaviour of the material under strong shear conditions, or in other words, under a highly erosive scenario. Although mechanical erosion is not expected to be the most relevant issue in terms of buffer degradation, the validation of the rheological model is a key point to account for gravity effects in the next section, as well as the contribution of wall friction to the expansion-erosion equilibrium (see case 4). Moreover, the numerical simulation of bentonite erosion under high water flow rates (for example tests 3 and 5 in Schatz et al. 2013, Table 20) has not yet been able to reproduce experimental results, except for the two-region model in Nerentieks et al. (2017). In this sense, Neretnieks et al. (2017) underestimated the amount of eroded mass in small-scale tests when using the original version of the model, whereas Schatz et al. (2013) overpredicted the pellet degradation in the same cases. The present section has thus focused on two highly erosive scenarios where chemical erosion, though existing, is not expected to increase the damage exerted by the flow. Case 4 will be especially interesting for analysing the intimate coupling between the rheological model and the wall friction term which allows a simultaneous quantification of erosion rate and expansion.

In all cases, the evolution of bentonite expansion has been tracked and validated with experimental data. The calculated values correspond to the expansion front, which is clearly visible due to the sharp gel and/or sol concentration gradient at the rim e.g., in Tests 5 and 6 by Schatz et al. (2013) (see Figure 6-10), but the experimental ones are subject to the presence of translucid dilute phases at the rim, which according to Figure 6-6 have not been included in the measurement by these authors (ibid.).

6.2.1 Case 3

This case corresponds to Test 3 in Schatz et al. (2013), which has the highest fracture water flow rate of all the scenarios considered (Table 3-1) and the shortest duration (19 days). The current model clearly underpredicts the expansion. However, after recalculating the case but considering an initial extrusion into the initial solution without any water flow during 24 h, the flow is not able to reduce the size of the bentonite disc (Figure 6-4). Therefore, it can be concluded that the erosion-expansion equilibrium is highly sensitive at this high flow regime. However, expansion is not precisely the critical factor in this case, as it will be always limited by the flow. The present simulation is mainly devoted to the performance of the rheological model in predicting mass losses due to mechanical erosion. In this sense, the model yields accurate results in terms of the final mass distribution in the system (Table 6-1).

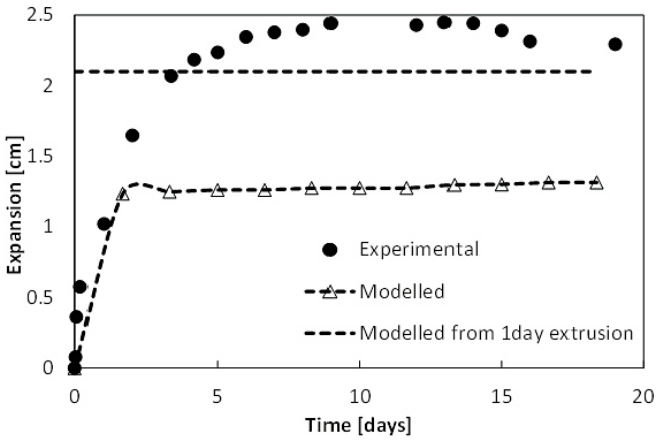

Figure 6-4. *Time evolution of bentonite expansion (in cm) during 19 days in case 3. Experimental values from Test 3 of Schatz et al. (2013).*

It should be noted that, at the current development stage, the motion/behavior of the detached flocs cannot yet be described by the model. Thus, it has been assumed that flocculation (though appearing) will not be able to withstand erosion and that flocs will be mostly dragged by the flow. This assumption is clearly conservative because the accumulation of flocs may protect the rim against further erosion to some extent. In fact, the model overpredicts the amount of eroded mass. The snapshots taken by Schatz et al. (2013) during the test show a dark flocculated mass surrounding the expanding disc. With available information, it cannot be distinguished whether these phases are being transported by the flow or at least a part remains attached to the rim, protecting further erosion. In any case, the role of flocculation in exerting shear resistance against bentonite expansion as presented in Neretnieks and Moreno (2018b) will be analyzed in the following cases.

Table 6-1. Final mass distribution in case 3 as given by the experiment and different modelling approaches. 2-reg. mod. = two region model.

	Remaining mass in pellet (g)	Eroded mass (g)
Experimental Schatz et al. (2013)	4.61	4.7
Neretnieks et al. (2017)	7	1.74
Neretnieks et al. (2017), 2-reg. mod., φ_R = 0.01	4.21	5.74
Neretnieks et al. (2017), 2-reg. mod., φ_R = 0.015	0	10
Schatz et al. (2013), BESW model	0.091	9.72
Current model	3.76	5.19
This work (initial extruded solution)	4.23	4.57

6.2.2 Case 4

This case corresponds to Test 5 in Schatz et al. (2013) (Table 3-1), which is equivalent to case 3 except for a slower water velocity (one order of magnitude). This has a direct consequence on the expansion-erosion balance. In the model, advective transport is not sufficient to provide a limited bentonite extrusion, which, however, has been observed experimentally. In this case, it is the action of the modelled wall friction term (Section 4.4.2) that stops the expansion front (Figure 6-5). It can be also observed that radial wall friction caused by detached flocs is located, as expected, at the rim. As stated in Section 4.4.2. the expanding paste will not experience shear resistance because DDL forces will prevent contact between smectite sheets and the fracture walls (Nerentieks et al. 2009).

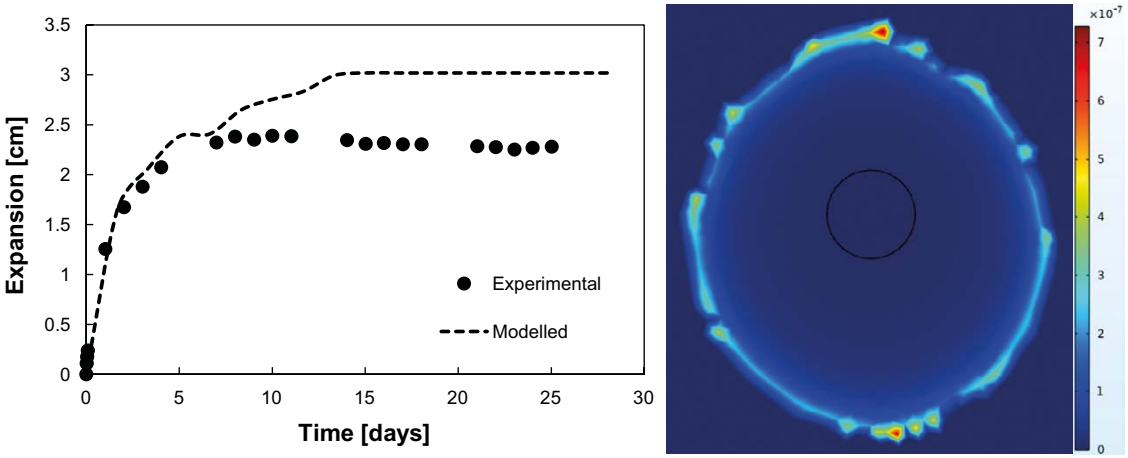

Figure 6-5. *Time evolution of bentonite expansion (in cm) in case 4 (left). Wall friction velocity $|\vec{w}|$ (m/s) after 720 h in case 4 (right).*

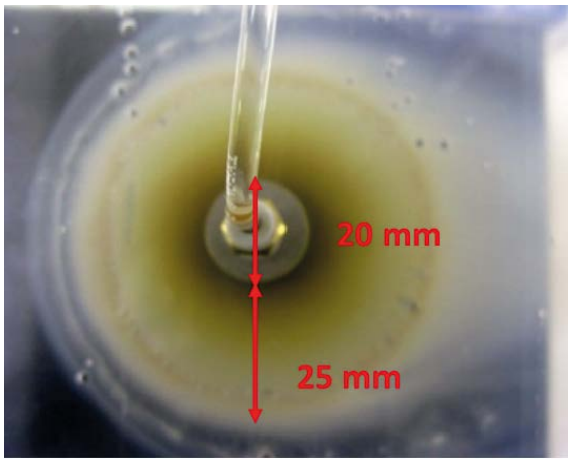

Figure 6-6. *Schematic representation of the extruded distance reported in Schatz et al. (2013, Test 5 at d) 168 h) for case 4, which is shown by the authors not to include the outer translucid phases.*

Still, this case constitutes a highly erosive flow scenario and up to 34 % of the initial bentonite mass is lost by erosion. Compared to all the models used to simulate this test, the current implementation provides the best prediction of both the remaining and eroded mass (Table 6-2). The Neretnieks model fails to capture erosion, whereas its implementation by Schatz et al. (2013) strongly overestimates expansion (Pont et al. 2020). On the other hand, the semi-empirical approach by Neretnieks et al. (2017) with a two-region model leads to acceptable results but shows high sensitivity with respect to the rim concentration parameter φ_R.

Table 6-2. Final mass distribution in case 4 as given by the experiment and different modelling approaches. 2-reg. mod. = two region model.

	Remaining mass in pellet (g)	Eroded mass (g)
Experimental	4.9	3.4
Neretnieks et al. (2017)	6.6	0.91
Neretnieks et al. (2017), 2-reg. mod., φ_R = 0.01	5.77	3.65
Neretnieks et al. (2017), 2-reg. mod., φ_R = 0.015	4.95	4.86
Schatz et al. (2013), BESW model	0.012	9.98
Current model	5	3.21

6.3 Quantification of bentonite mass losses due to chemical erosion and gravity

After having tested the rheological and the wall friction models in highly erosive scenarios with 1 mm fractures, their performance must be evaluated in smaller apertures, sloping fractures and slower flow regimes. This will allow assessing the effect of flocculation and gravity when conditions approach those of a bentonite buffer in a nuclear waste repository. In this section, four different small-scale tests have been simulated and the performance of the complete model presented in Section 4 has been evaluated.

6.3.1 Case 5

This case corresponds to Test 6 in Schatz et al. (2013) (Table 3-1). It is similar to case 4, except for the water composition (Grimsel groundwater simulant instead of deionized water) and the flow rate, which is approximately four times smaller. This means that mechanical erosion might not be enough to explain the observed mass loss rate and the expansion-erosion equilibrium. This is precisely the outcome of the model (see gray curve in Figure 6-7), which overpredicts expansion even when considering wall friction. This suggests that losses due to chemical erosion needs to be included in the model. To this end, the constant of the sink term implemented for this purpose needs to be calibrated (Section 4.4.4). This calibration is based on the adjustment of the bentonite expansion curve in Figure 6-7, which leads to a value of $C = 50$. Then, the total erosion rate, including mechanical and chemical erosion, has been calculated and compared to the experimental measurements, showing a very good agreement (Table 6-3). Figure 6-8 shows the evolution of the flocculation rate per unit volume at three different times. However, the final mass distribution, although acceptable, is not as precise as in case 4 (Figure 6-9). This slight disagreement might have to do with the fate of the detached colloids, which might locally reassemble in flocs at the expansion front at an advanced stage of the test. This phenomenon is observed in Figure 6-9, where the final experimental extrusion profile shows a non-negligible mass accumulation at the rim and will become more important in the following two cases with 0.1 mm fracture aperture. However, in the present 1 mm fracture, the average erosion rate has not been affected by this issue (Table 6-3).

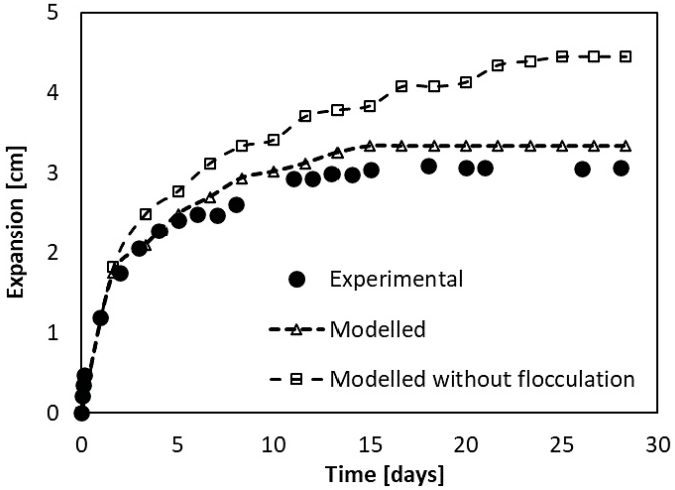

Figure 6-7. *Time evolution of expansion radius from the hole wall in case 5.*

Table 6-3. Final mass distribution and average erosion rate in case 5 as given by the experiment and different modelling approaches. 2-reg. mod. = two region model.

	Remaining mass in pellet (g)	Eroded mass (g)	Average erosion rate (kg/s)
Experimental	5.72	2.4	1.0×10^{-9}
Neretnieks et al. (2017)	6.4	0.34	-
Neretnieks et al. (2017), 2-reg. mod., $\varphi_R = 0.01$	6.35	0.59	-
Neretnieks et al. (2017), 2-reg. mod., $\varphi_R = 0.015$	6.05	2.18	-
Current model	5.25	3.3	1.0×10^{-9}

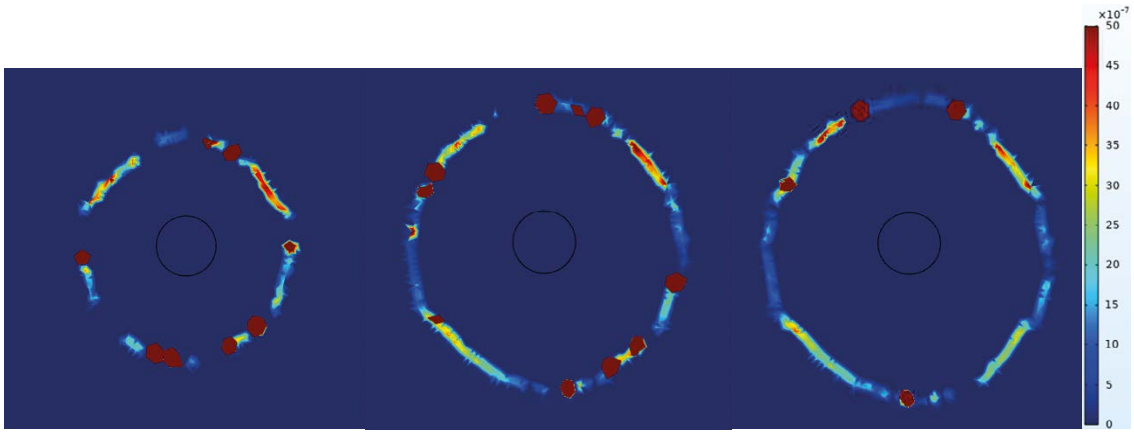

Figure 6-8. *Flocculation rate per unit volume $\rho_S R_{floc} \varphi$ ($kg \cdot m^{-3} \cdot s^{-1}$) after 5, 15, and 28 days in case 5.*

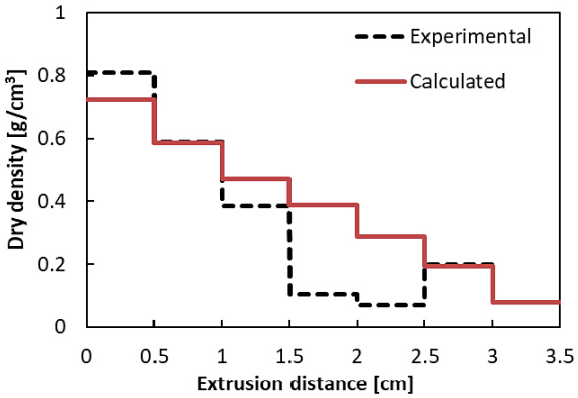

Figure 6-9. *Final smectite extrusion density profile after 28 days corresponding to case 5, in terms of bentonite dry density (g/cm^3). The zero value in the x-axis corresponds to the bentonite pellet surface.*

6.3.2 Case 6

This case is equivalent to the previous one but with a 45º sloping fracture (Schatz and Akhanoba 2017) (see Table 3-1). It introduces a new erosion mode due to gravity, included in the model as a volume force in the Stokes equations. In the model, the extruded smectite is treated as a continuum. Individual particles or flocs cannot be yet considered as independent entities with their own motion. It is assumed that colloids are detached when gravity-increased shear overcomes the cohesive forces between smectite sheets. In reality, gravity only enhances the transport of chemically eroded colloids away from the rim. This analogy has, of course, its limitations (see cases with 0.1 mm fractures) but provides a proper quantification of the total erosion rate. It should be noted that the rheological properties of smectite sol (less than 3 %wt.) strongly depend on sodium concentration, for which mechanics and chemistry are tightly coupled.

The effect of the fracture slope in form of a sedimentation cascade can be clearly observed in Figure 6-10, where the shape of the bentonite extrusion is compared to that of case 5 and to the experimental counterpart.

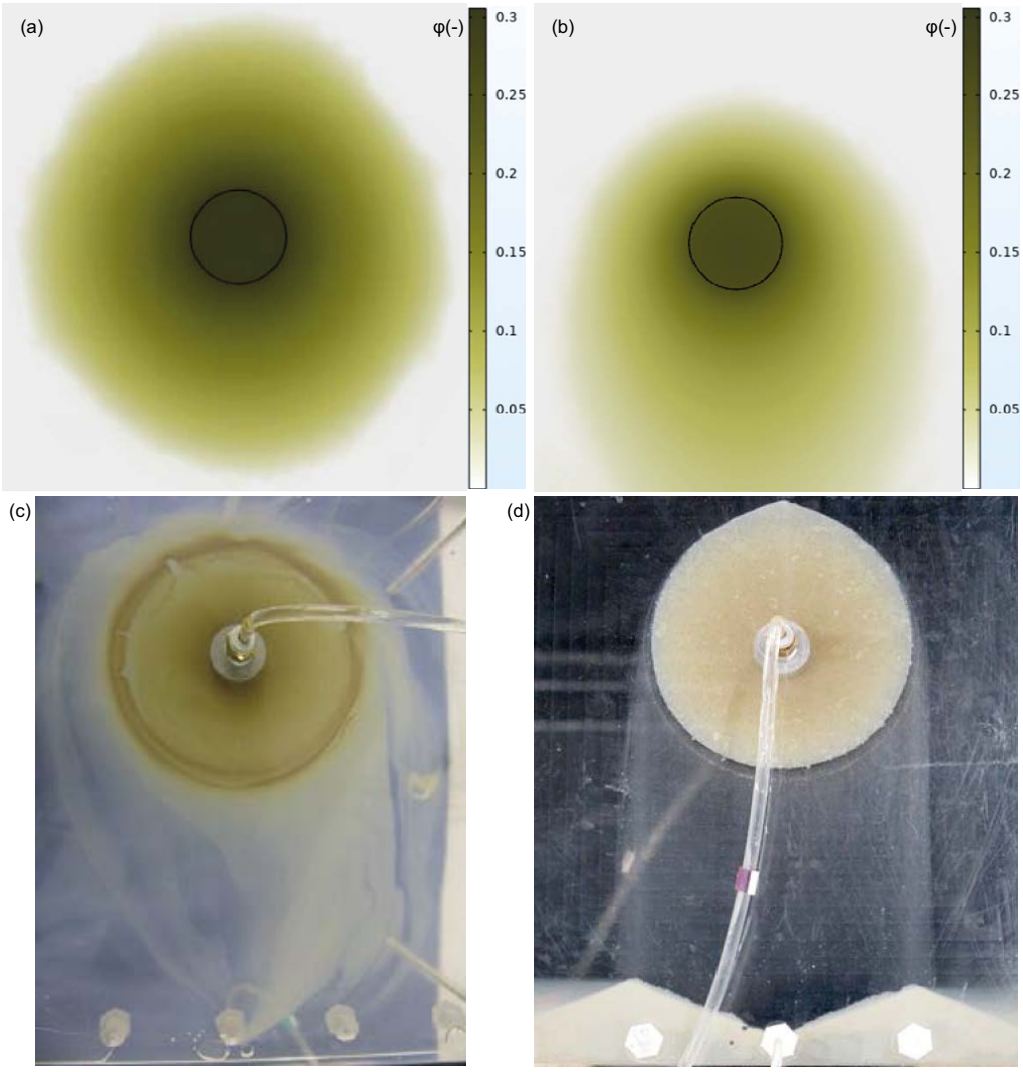

Figure 6-10. *Calculated smectite volume fraction (φ) in Test 5 at t = 672 h (a) and in case in Figure 3-3 at t = 480 h (b). Experimental Na-bentonite expansion at the same times in Test 5 (c) and case in Figure 3-3 (d) presented by Schatz et al. (2013) and Schatz and Akhanoba (2017), respectively.*

The main feature of this case is the degradation of the expanded bentonite disc due to the erosive effect of gravity. This is observed in the experimental test with a reduction of the extrusion distance after approximately 250 hours (Figure 6-11). The model reproduces the onset of degradation quite accurately, as well as the total erosion rate (Table 6-4). However, the interaction between the wall friction term and the falling sedimentation poses a relevant issue. The model is not capable of distinguishing between gel flocs at the rim, where the wall friction term is clearly acting (Figure 6-5 right), and colloids falling down without getting structured into a gel that can really exert a certain shear resistance to motion. This leads to a reduction of the erosion rate when wall friction is considered (Table 6-4). A brief discussion on this topic is included in Section 8.

Table 6-4. Average erosion rate (kg/s) in case 6.

	Average erosion rate ($kg \cdot s^{-1}$)
Experimental (case 6)	1.86×10^{-9}
Current model (with wall friction)	1.20×10^{-9}
Current model (no wall friction)	1.87×10^{-9}

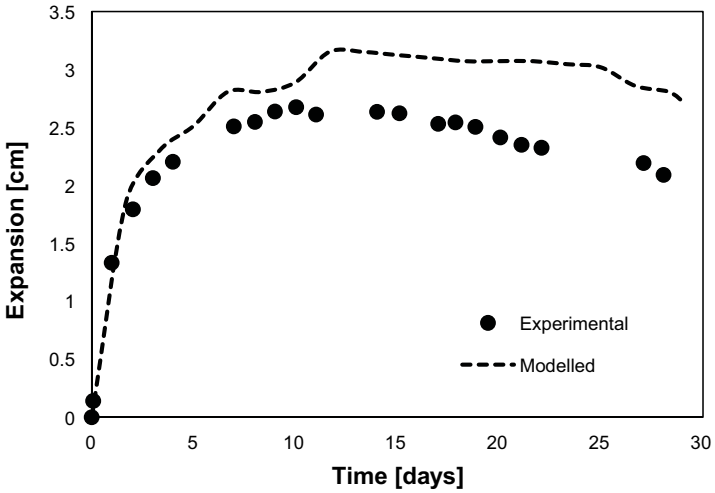

Figure 6-11. *Time evolution of expansion (in cm) of bentonite volume fraction (φ) in case 6 reported in Schatz and Akhanoba (2017, Test 2).*

6.3.3 Case 7

This case corresponds to Test 2 in Appendix D (see Table 3-1). Its main interest lays on a narrower fracture aperture (0.1 mm). The goals are to test the wall friction scaling proposed in Section 4.4.3 and to quantify the dependency between this magnitude and the erosion rate due to gravity. The volume of the initial bentonite in Test 2 was, however, much smaller than in Test 1 (ibid.), leading to a smaller extrusion radius. To this end, the results of case 4 will be used as a reference because of its similar water flow rate, initial bentonite dry density, and sodium concentration in the flowing water. Although the present fracture slope is vertical instead of tilted 45°, Schatz and Akhanoba (2017) observed only small differences in the erosion rate between these two slopes.

As can be observed in Figure 6-12, the model manages to reproduce quite accurately the evolution of expansion experimentally measured. On the other hand, wall friction has not interfered in the sedimentation due to gravity as it did in the previous 1 mm aperture. This fact might be related to the theoretically linear relation between sedimentation rate and fracture aperture (Schatz and Akhanoba 2017). The outcome of the simulation, accounting for all three erosion modes, confirms this hypothesis (Table 6-5). However, the experimental measurements show a much smaller value. In this sense, Figure 6-13 might explain the reason of this significant mismatch. From the very beginning, the experimental erosion rate decreases because the flocs get trapped in the fracture by the formation of a consistent secondary gel. This phenomenon, which had not been found in the 1 mm fractures, where a free-falling colloid cascade can be seen (Figure 6-10), has been observed in several experimental tests (Appendix D). However, it cannot be captured by the model at the current stage of development. In case 7, the fracture is narrow enough to allow material accumulation and consolidation between the walls, leading to a harsh reduction of mass reaching the downstream. This issue is further discussed in Section 8.

Table 6-5. Average erosion rate (kg/s) in case 7.

	Average erosion rate ($kg \cdot s^{-1}$)
Experimental, case 7	3.52×10^{-11}
Current model, case 6	1.87×10^{-9}
Current model, case 7	2.12×10^{-10}

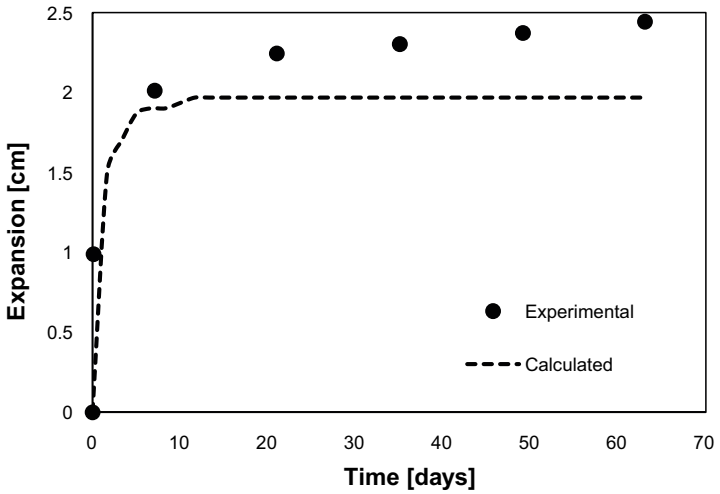

Figure 6-12. *Time evolution of expansion (in cm) of bentonite volume fraction (φ) in case 7 reported in Appendix D (Test 2).*

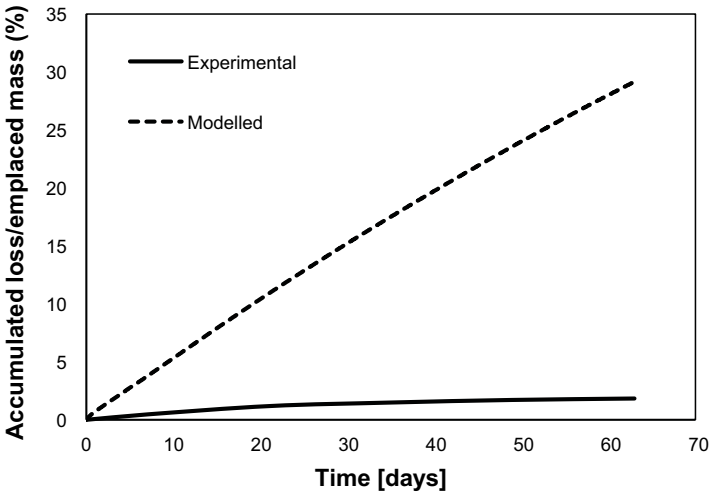

Figure 6-13. *Time evolution of the relative accumulated mass loss in case 7.*

6.3.4 Case 8

This case corresponds to Test 5 in Appendix D (see Table 3-1). The main difference is the initial bentonite dry density, which is significantly lower than all previous cases (1.1 $g \cdot cm^{-3}$). However, the wall friction model is again capable of providing an approximate limitation of bentonite expansion (Figure 6-14). Regarding erosion, the calculated mass loss rate is also one order of magnitude smaller than in case 6 (Table 6-6), whereas the experimental value also shows the evidence of secondary gel accumulating in the fracture (Table 6-7) like in the previous test.

Table 6-6. Average erosion rate (kg/s) in case 8 compared to case 6.

Calculated, case 6	1.87×10^{-9}
Calculated, case 8	2.9×10^{-10}

Table 6-7. Relative accumulated mass loss (%) in case 8.

Calculated	35
Experimental	1.3

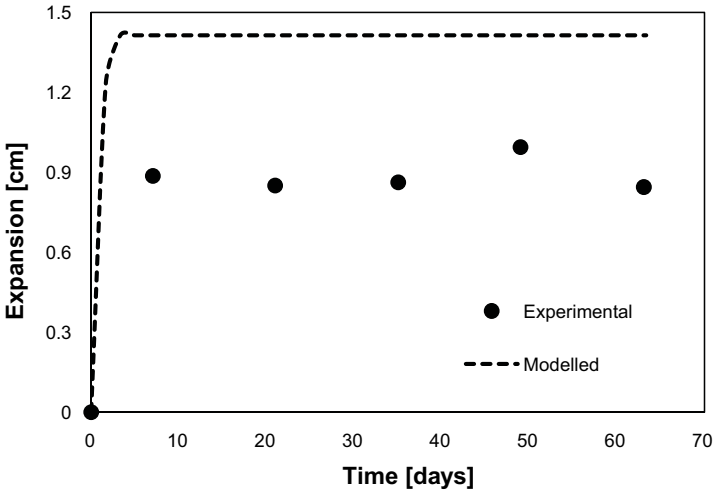

Figure 6-14. *Time evolution of expansion (in cm) of bentonite volume fraction (φ) in case 8 reported in Appendix D (Test 5).*

7 Results – repository scale model

The conceptual model presented in Section 4 and tested in Section 6 is applied here to the Performance Assessment of the bentonite buffer in the KBS-3 repository under the effect of a single intersecting fracture with flowing glacial meltwater. The final goal consists in providing a best estimate of the buffer degradation process due to mechanical erosion (negligible in hydraulic conditions of very low flow rates), chemical erosion, and sedimentation in critical scenarios involving water salinity below CCC (1 mM Na) and low calcium sorption. As observed in small-scale tests, these chemical conditions can lead to significant clay mass losses, but the upscaling to repository dimensions assuming normalized erosion rates per unit surface of buffer-fracture interface is not straightforward. In this sense, Smith et al. (2017) indicate that using this upscaling method, erosion rates of 1 $kg \cdot yr^{-1}$ may be reached in 4 % of the supercontainer sections in the KBS-3H repository concept in Olkiluoto after 1 000 years of glacial conditions, although several uncertainties still need to be addressed. For this reason, three cases presented in Table 3-2 covering a wide range of groundwater flow rates, two different fracture apertures, and both horizontal and sloping fractures have been simulated.

As commented in Section 5.2, the increase in computational cost with respect to the short small-scale tests calculated in Section 6 has limited both mesh refinement and the total simulation time that can be considered. Simulations up to 100 000 years is unaffordable at the current stage of development, and therefore they have been restricted to only 10 or 100 years from the onset of glacial meltwater arrival (Table 3-2), up to the time needed for expansion and erosion to reach pseudo-steady state conditions. Then, the impact of the calculated erosion rate at an observation point located on the fracture plane 10 cm inside the buffer has been extrapolated up to a critical dry density of 1 000 $kg \cdot m^{-3}$, which is the expected value below which the risk of advective transport in the buffer increases (Smith et al. 2017). This threshold has been used as buffer integrity limit in all simulated cases. The results obtained must be considered as preliminary and a first approximation towards a complete performance assessment of the bentonite buffer in a KBS-3 repository concept accounting for the long-term effect of wall friction, chemical erosion, and sedimentation.

7.1 Case 1

Case 1 has been selected as a worst-case scenario in terms of mechanical erosion. It assumes the highest flow velocity (10^{-5} $m \cdot s^{-1}$) of the three cases, far above the expected conditions in the repository and a single 1 mm aperture horizontal fracture. However, this case, together with case 2, provide a deeper insight of the flow model performance with respect to computational results using the Darcy-based KTH model reported by Schatz et al. (2013).

Due to the highly advective conditions, an early equilibrium between expansion and erosion rate is met in this case (Figure 7-1). For this reason, wall friction has not been considered nor the effect of flocculation, which compared to mechanical erosion due to shear, is assumed to be negligible like in Cases 3 and 4 of Section 6. These simplifications have led to a significant reduction of the computational cost.

A steady erosion rate of 256 $g \cdot yr^{-1}$ is reached after very few hours (Figure 7-2). This value is slightly smaller than the 292 g/yr estimated by Schatz et al. (2013) using the original KTH model (Table 7-1). However, the critical dry density is reached after only 6 500 years in the current model. It can be concluded that the implemented rheological model and the Stokes equations for flow applied to a 3D domain constitute a less conservative approach to the quantification of bentonite mass losses due to fracture flow than the Darcy-based KTH model (Moreno et al. 2010). In terms of clay expansion, both approaches yield similar results due to the dominance of flow erosion.

Table 7-1. Expansion-erosion pseudo-equilibrium for case 1.

Result	Schatz et al. (2013)*	Current model
Final expansion (m)	0.5	0.55
Erosion rate (g/yr)	292	256.0

* Simulation performed with the model by Moreno et al. (2010).

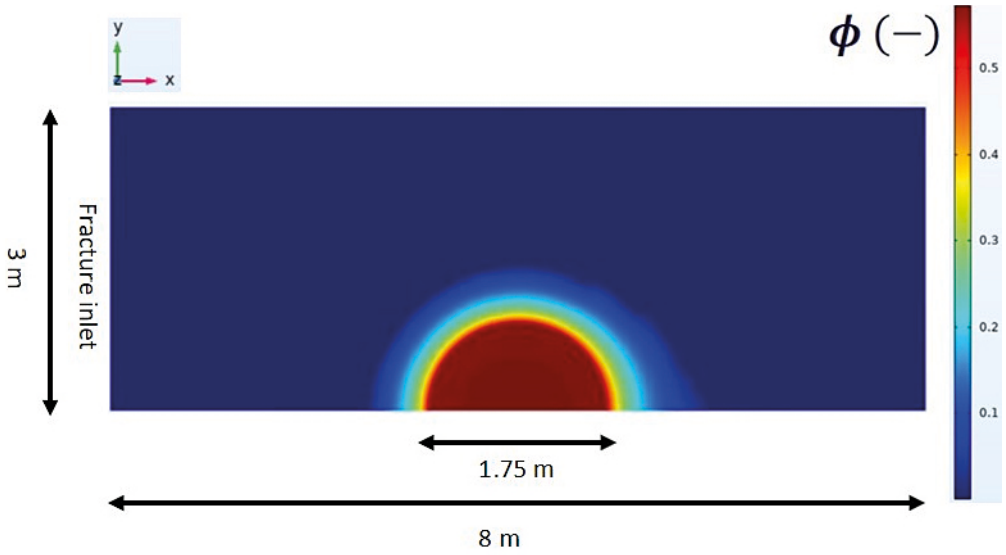

Figure 7-1. *Smectite volume fraction (-) profile on the fracture plane after 100 years for case 1.*

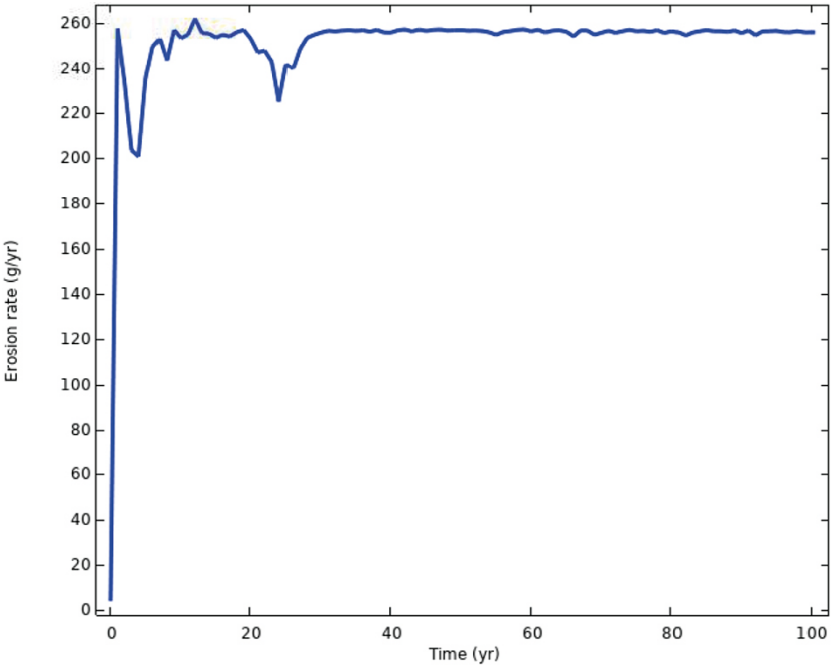

Figure 7-2. *Erosion rate evolution modelled as bentonite mass flow rate at the fracture outlet for case 1.*

7.2 Case 2

Case 2 aims at evaluating the sensitivity of the model to water flow velocity, which is reduced by one order of magnitude with respect to case 1. Again, only mechanical erosion has been considered because losses due to flocculation are still expected to be negligible in front of flow erosion. As expected, the pseudo-equilibrium between erosion and expansion is represented by a larger contribution of expansion if compared to case 1, reaching in case 2 nearly a steady value of 1.5 m on the *y*-axis (Figure 7-3). The pseudo-equilibrium between expansion and erosion is reached much later than in case 1, namely after ~80 years. The critical dry density is expected to be reached after 19 000 years. Again, the model yields a slightly lower erosion rate than the KTH model used in Schatz et al. (2013) (Table 7-2).

Regarding expansion, the current model yields a more moderate prediction (Table 7-2). The reason behind this reduction might be the BESW approximation of the smectite diffusion coefficient (Liu et al. 2009) implemented by Schatz et al. (2013), which is prone to overestimate bentonite extrusion (Pont et al. 2020).

Table 7-2. Expansion-erosion pseudo-equilibrium for case 2.

Result	Schatz et al. (2013)*	Current model
Final expansion (m)	2.1	1.47
Erosion rate (g/yr)	117	113.6

* Simulation performed with the model by Moreno et al. (2010).

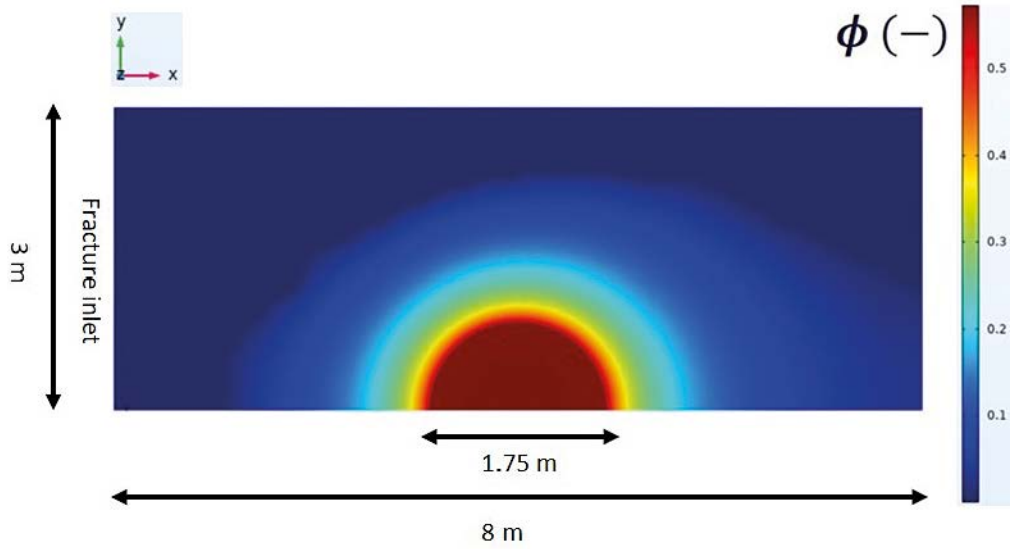

Figure 7-3. *Smectite volume fraction (-) profile on the fracture plane after 100 years for case 2.*

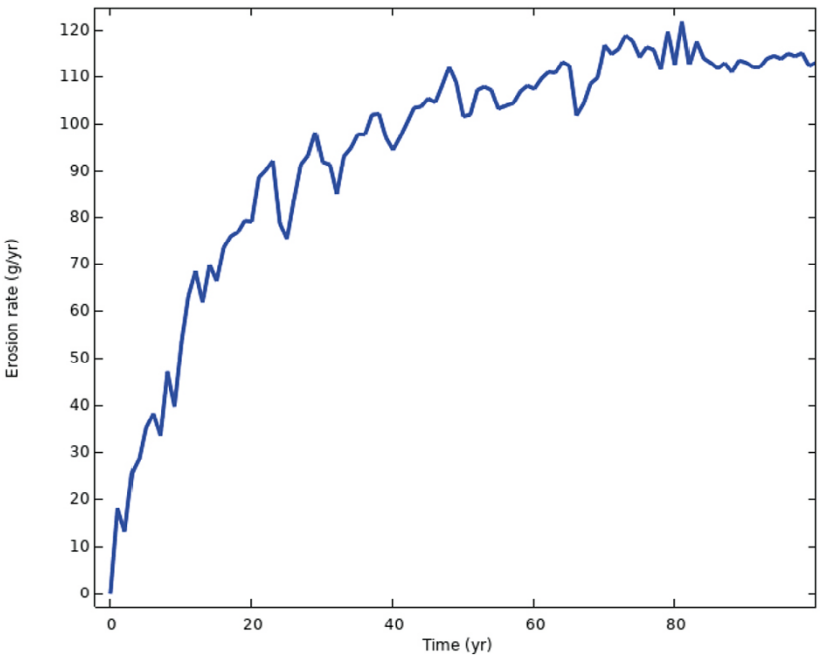

Figure 7-4. *Erosion rate evolution measured as bentonite mass flow rate at the fracture outlet for case 2.*

7.3 Case 3

Case 3 aims at reproducing a realistic scenario in terms of the expected repository conditions. It considers a significantly lower fracture flow velocity (3×10^{-8} m·s^{-1}) compared to the previous cases, closer to repository conditions (Sena et al. 2010). Schatz and Akhanoba (2017) experimentally showed that this variation in the water flow rate is not expected to have a relevant impact on the total erosion rate in small-scale tests, which will be now clearly driven by chemical erosion and sedimentation due to gravity. As observed in Section 6, this leads to a more relevant impact of wall friction and flocculation in the equilibrium between expansion and erosion. The former will reduce clay extrusion and its interaction with the water in the fracture. On the other hand, the latter will favour clay losses into the seeping water. Moreover, case 3 introduces two new relevant factors in the present analysis: a 45° fracture slope and a narrower fracture aperture (0.4 mm). For all these reasons, this new scenario requires the application of the full model presented in Section 4, but at the expense of a limited simulation time (10 years) due to the substantial increase in computational cost.

In this case, bentonite extrusion in the fracture is limited to few centimetres due to the combined action of gravity, flocculation, and wall friction (Figure 7-5). One could expect a higher erosion rate as the reason behind such a low expansivity. However, Table 7-3 shows rather the contrary: the erosion rate (~100 g/yr) is very similar to case 2. This erosion rate is significantly lower than the one predicted by Smith et al. (2017) using an upscaling method based on the erosion rate per interfacial area measured in small-scale tests, which yielded values between 500–1 000 g/yr. Moreover, one must also consider that the estimations by Smith et al. (2017) correspond to 0.1 mm fractures, whereas the present one is referred to an aperture of 0.4 mm. This means that, as shown in Section 6, the erosion rate predicted by the model would diminish by a factor of ~4 if the model were applied to a 0.1 mm fracture. In this case, one should also expect clogging due to secondary gel formation, which would further reduce the erosion rate. Unfortunately, this configuration has not yet been tested with the current model due to solver convergence issues related with excessive element stretching.

Due to high computational cost, the present case has been restricted to a simulation time of 10 years. According to Figure 7-6, the erosion rate has not yet reached a steady value, although the pseudo-equilibrium is expected to be met at an early stage. Therefore, the final value of in the order of 100 g/yr has been obtained extrapolating a non-linear 5PL regression curve. Another interesting feature is that unlike the previous two cases, which follow convex erosion curves, case 3 shows a concave evolution with an initial maximum. This might be related to the presence of the gravity force, which might lead to a numerical transient before the wall friction term becomes effective. However, this is not expected to alter the final value of the long-term erosion rate.

Table 7-3. Expansion-erosion pseudo-equilibrium for case 3.

Result	Current model
Final expansion (m)	0.125 (maximum)
Erosion rate (g/yr)	~100

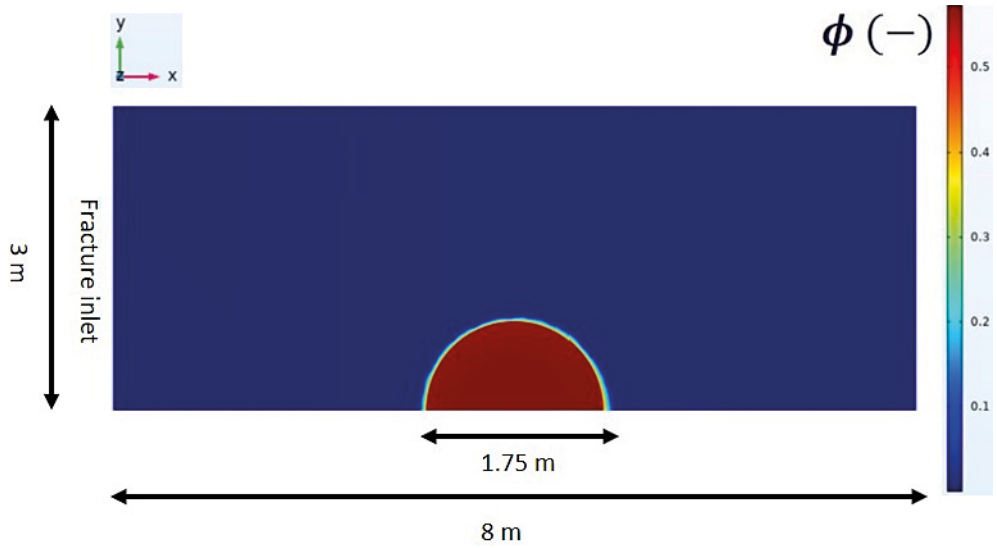

Figure 7-5. *Smectite volume fraction (-) profile on the fracture plane after 10 years for case 3.*

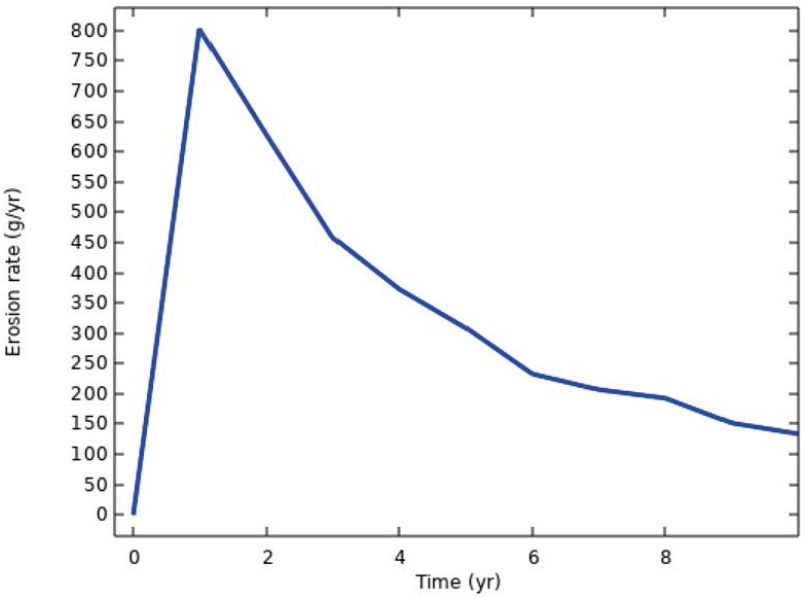

Figure 7-6. *Erosion rate evolution measured as bentonite mass flow rate at the fracture outlet for case 3.*

8 Discussion and conclusions

8.1 Discussion – model limitations and remaining uncertainties

The presented wall friction and non-linear creeping flow models have been able to describe the expansive behaviour of smectite in a wide range of small-scale tests. The chemical conditions of these tests are expected to be relevant in the long-term safety analysis for buffer integrity in presence of glacial groundwater. However, the second calibration test presented in Section 6.1 adds some uncertainty, since the model is not able to limit expansion into a 0.2 mm fracture with stagnant water, as experimentally observed in Alonso et al. (2019). This disagreement has not been observed in the 1 mm fracture. For this reason, the discussion presented in Pont et al. (2020) around a hypothetical combination of two different wall friction types – a viscous one, as already included in the model, and a dry one exerted by the expanding paste against the wall – is still open.

The speculation formulated in Pont et al. (2020) and in Appendix B regarding the relevance of surface tension effects in narrow fractures could also explain, at least in part, the disagreement between the model and the experimental results. But confirmation of this would require further modelling efforts in this direction. In this regard, the value of the interfacial tension between dilute smectite gel and water is subject to a high degree of uncertainty (Jańczuk et al. 1996). As stated in Section 6.1, the rheology of bentonite is highly dependent on its composition, treatment, and aging, for which the parameter $\dot{\gamma}_0$ of the clay used to model the test of Alonso et al. (2019) should also be further assessed.

Although most uncertainties concerning chemical erosion and gravity have been properly addressed by the model, fracture clogging due to flocs forming a secondary gel in narrow fractures (0.1 mm) with low seeping water flow rates has not been assessed. As shown in Section 6.3, this phenomenon may play an important role in preventing bentonite expansion and erosion in these cases. Even though the limitation of expansion is properly predicted by the model, the erosion rate reduction due to the accumulation of mass beyond the expansion front is yet to be analysed, as well as its significance in preventing buffer degradation. At this point, the coupling with a geochemical model accounting for ionic exchange, as presented in Pont et al. (2020), could provide a better assessment of the long-term consistency of this gel. In turn, this would also allow considering the effect of accessory minerals, which are thought to enhance buffer integrity due to their calcium content (Bouby et al. 2020).

Finally, the interaction between gravity driven sedimentation and the proposed wall friction term needs to be further assessed, as evidenced by case 6. With the current state of the model, one cannot distinguish the mechanically consistent gel at the rim from falling colloids due to gravity, leading to a reduced erosion rate downstream. In this sense, an alternative derivation of the wall friction term as a boundary condition at the rim is currently being evaluated (Appendix C).

8.2 Conclusions

An extension of the KTH model affecting the flow equations and the smectite expansion equation (Liu et al. 2009) has been proposed to reduce the disagreements between numerical models and experimental results in terms of bentonite expansion and erosion. The flow and smectite transport equations have been extended with explicit consideration of viscous shear stress, wall friction, and chemical erosion.

Given the disagreements between experimental results of bentonite expansion within fractures (Schatz et al. 2013, Schatz and Akhanoba 2017, Alonso et al. 2019, and Appendix D) and the KTH model (Neretnieks et al. 2017), a wall friction model was first presented in Pont et al. (2020). This model is based on viscous shear stress exerted by segregated gel at the rim and has been included in the smectite expansion equation. This approach reproduces the wall friction concept proposed by Neretnieks and Moreno (2018b), which restricts this effect to shear resistance of the segregated gel that appears at the rim when ionic strength drops below CCC and calcium absorption remains low. The model has been able to adjust the experimental results regarding expansion for a wide spectrum of small-scale tests (Section 6). Together with the implemented rheological model in the flow equations, it provides a good approximation of the equilibrium between expansion and mechanical erosion (Section 6.2). The only exception has been case 2 (Section 6.1) with stagnant water in a 0.2 mm fracture, as discussed in the previous section.

The other major concerns regarding long-term integrity of the bentonite buffer in the KBS-3 concept are (1) sedimentation due to flocculation (chemical erosion) and (2) gravity in sloping fractures. These two phenomena have been modelled and tested in Section 6.3. The flocculation rate implemented as a sink term in the smectite expansion equation, together with the applied volumetric gravity force, has provided a satisfactory quantification of the total erosion rate in scenarios with low water flow rate with concentrations below CCC. In this sense, the dependencies between erosion rate and fracture aperture and slope presented in Schatz and Akhanoba (2017) and Smith et al. (2017) have been properly quantified by the model. At the same time, the combined effect of these two modelled sedimentation modes with the presented wall friction term has led to a proper description of the expansion evolution in all cases.

However, as expected, the model is not able to accurately predict the erosion rate in 0.1 mm fractures. In these cases, accumulation of flocs in the fracture under the form of a secondary gel are observed in several experimental tests. The consistency of this gel, unlike the free-falling colloids observed in 1 mm fractures, poses an interesting issue regarding the long-term integrity of the buffer.

Overall, the model describes all three relevant erosion modes independently with a coupled set of governing equations. This implementation methodology has several advantages. First, it allows a physically consistent description of bentonite expansion and erosion. Furthermore, it enables a separate quantification of each mechanism independently. Finally, the model can be easily simplified when one of the mechanisms is not expected to play a significant role.

Finally, in Section 7 the model was applied to realistic repository scenarios to assess the integrity of the buffer after the intrusion of glacial meltwater. Both horizontal and sloping fractures have been simulated with promising results. On one hand, the performance of the rheological model under highly erosive flows in 1 mm fractures has provided a significant reduction of the erosion rate with respect to the KTH model (Schatz et al. 2013). On the other hand, the application of the full model to a 0.4 mm sloping fracture has also led to a more optimistic result than the upscaling method presented by Smith et al. (2017). In the latter, the erosion rate has been reduced from 500–1 000 g/yr in a 0.1 mm fracture to 28.6 g/yr in a 0.4 mm one, with which the critical density of the buffer would be reached after ~19 000 years. Results from small-scale tests (Section 6) indicate that the erosion rate would decrease linearly with the fracture aperture (a factor of 4 decrease in erosion rate when reducing the fracture aperture from 0.4 to 0.1 mm). Moreover, clogging effects due to secondary gel formation still need to be conceptualized and quantified.

8.3 Future work

The uncertainties discussed in Section 8.1 are part of possible future development stages. The current outcomes of the model show that, under certain circumstances, it provides an excessively conservative estimation of the eroded mass. In this sense, ionic exchange between clay and groundwater assuming Donnan equilibrium could be implemented as done in Pont et al. (2020), to evaluate the extent of Ca-enrichment of interlayer water, which is known to reduce both expansion and flocculation. Moreover, the description of secondary gel formation and the subsequent fracture clogging could also be included in the model for the same reason, as observed in cases 7 and 8. To this end, a second smectite transport problem accounting for the segregated flocs, their motion and interaction could be used.

All these developments would lead to a significantly more complex model, for which it might only be suited for short small-scale erosion tests due to computational cost issues. This limitation requires a simplification process that condenses the modelled coupled processes into an analytical expression for the erosion rate that could be easily upscaled to repository conditions for scoping calculations. This tool is envisaged as the final development stage of the model.

In the short term, the optimization of the numerical solver could be addressed. On one hand, this would enhance the robustness of the model and its application to narrow fractures, which require a finer spatial discretization at the bentonite-water interface. On the other, this would allow the simulation of a larger set of small-scale tests for a more thorough validation of the model. In this sense, the calibration of the model with other experimental setups using different types of bentonite, as well as the effect of interfacial forces in narrow fractures with stagnant water, like case 2 in Section 6, are two relevant sources of uncertainty that could also be addressed in the future.

References

SKB's (Svensk Kärnbränslehantering AB) publications can be found at www.skb.com/publications. Posiva's publications can be found at https://www.posiva.fi/en/index/media/reports.html.

Adachi Y, Nakaishi K, Tamaki M, 1998. Viscosity of dilute suspension of sodium montmorillonite in an electrostatically stable condition. Journal of Colloid and Interface Science 198, 100–105.

Ahn J, Chambré P L, Verbeke J, 1999. Numerical simulation of bentonite extrusion through a narrow planar space. MRS Online Proceedings Library Archive, 608. doi:10.1557/PROC-608-185

Alonso U, Missana T, García Gutiérrez M, Morejón J, Mingarro M, Fernández A, 2019. CIEMAT studies within POSKBAR project. Bentonite expansion, sedimentation and erosion in artificial fractures. SKB TR-19-08, Svensk Kärnbränslehantering AB.

Arthur R, 2011. Handling of hydrogeochemical relations in erosion and swelling pressure models for the buffer and backfill. Part I: A review of surface-chemical concepts used in models of buffer erosion. STUK-TR 10, Radiation and Nuclear Safety Authority (STUK).

Birgersson M, Karnland O, 2009. Ion equilibrium between montmorillonite interlayer space and external solution – Consequences for diffusional transport. Geochimica et Cosmochimica Acta, 73, 1908–1923.

Birgersson M, Börgesson L, Hedström M, Karnland O, Nilsson U, 2009. Bentonite erosion. Final report. SKB TR-09-34, Svensk Kärnbränslehantering AB.

Borrelli R A, Ahn J, 2008. Numerical modeling of bentonite extrusion and radionuclide migration in a saturated planar fracture. Physics and Chemistry of the Earth, Parts A/B/C 33, S131–S141.

Bouby M, Kraft S, Kuschel S, Geyer F, Moisei-Rabung S, Schäfer T, Geckeis H, 2020. Erosion dynamics of compacted raw or homoionic MX-80 bentonite in a low ionic strength synthetic water under quasi-stagnant flow conditions. Applied Clay Science 198, 105797. doi:10.1016/j.clay.2020.105797

Börgesson L, Hedström M, Birgesson M, Karnland O, 2018. Bentonite swelling into fractures at conditions above the critical coagulation concentration. SKB TR-17-11, Svensk Kärnbränslehantering AB.

COMSOL, 2018. COMSOL Multiphysics® v. 5.4. COMSOL AB, Sweden.

Convery N, Gadegaard N, 2019. 30 years of microfluidics. Micro and Nano Engineering 2, 76–91.

Gens A, 2010. Soil-environment interactions in geotechnical engineering. Géotechnique 60, 3–74.

Girifalco L A, Good R J, 1957. A theory for the estimation of surface and interfacial energies. I. Derivation and application to interfacial tension. The Journal of Physical Chemistry 61, 904–909.

Islam M N, Bunger A P, Huerta N, Dilmore R, 2019. Bentonite extrusion into near-borehole fracture. Geosciences 9, 495.

Jańczuk B, Bruque J M, González-Martín M L, Del Pozo J M, Zdziennicka A, Quintana-Gragera F, 1996. The usefulness of the equation of state for interfacial tensions estimation in some liquid-liquid and solid-liquid systems. Journal of Colloid and Interface Science 181, 108–117.

Kanno T, Iwata Y, Sugino H, 2001. Modelling of bentonite swelling as solid particle diffusion. In Adachi K, Fukue M (eds). Clay science for engineering. Boca Raton, FL: CRC Press, 561–570.

Laviña M, Idiart A, Molinero J, Casas G, 2018. POSKBAR project. Development, testing and application of alternative models for bentonite expansion and erosion. SKB TR-17-13, Svensk Kärnbränslehantering AB.

Liu, L, 2010. Permeability and expansibility of sodium bentonite in dilute solutions. Colloids and Surfaces A: Physicochemical and Engineering Aspects 358, 68–78.

Liu L, Neretnieks I, 2006. Physical and chemical stability of the bentonite buffer. SKB R-06-103, Svensk Kärnbränslehantering AB.

Liu L, Moreno L, Neretnieks I, 2009. A dynamic force balance model for colloidal expansion and its DLVO-based application. Langmuir 25, 679–687.

Mason M, Weaver W, 1924. The settling of small particles in a fluid. Physical Review 23, 412–426.

Moreno L, Neretnieks I, Liu L, 2010. Modelling of erosion of bentonite gel by gel/sol flow. SKB TR-10-64, Svensk Kärnbränslehantering AB.

Neretnieks I, Moreno L, 2018a. Revisiting bentonite erosion understanding and modelling based on the BELBaR project findings. SKB TR-17-12, Svensk Kärnbränslehantering AB.

Neretnieks I, Moreno L, 2018b. Some mechanisms that influence bentonite erosion in a KBS-3 repository – an exploratory study. SKB TR-18-13, Svensk Kärnbränslehantering AB.

Neretnieks I, Moreno L, 2021. Ion composition at bentonite-water interface and its impact on erosion. SKB P-20-26, Svensk Kärnbränslehantering AB.

Neretnieks I, Liu L, Moreno L, 2009. Mechanisms and models for bentonite erosion. SKB TR-09-35, Svensk Kärnbränslehantering AB.

Neretnieks I, Moreno L, Liu L, 2017. Clay erosion – impact of flocculation and gravitation. SKB TR-16-11, Svensk Kärnbränslehantering AB.

Pont A, Coene E, Idiart A, 2020. Bentonite erosion project. Preliminary study for the numerical simulation of bentonite erosion. SKB P-20-16, Svensk Kärnbränslehantering AB.

Pujala R K, 2014. Dispersion stability, microstructure and phase transition of anisotropic nanodiscs. Cham, Switzerland: Springer International Publishing.

Richards T, 2010. Particle clogging in porous media. Filtration of a smectite solution. SKB TR-10-22, Svensk Kärnbränslehantering AB.

Sato D, Kobayashi M, Adachi Y, 2004. Effect of floc structure on the rate of shear coagulation. Journal of Colloid and Interface Science 272, 345–351.

Schatz T, Akhanoba N, 2017. Bentonite buffer erosion in sloped fracture environments. Posiva 2016-13, Posiva Oy.

Schatz T, Kanerva N, Martikainen J, Sane P, Olin M, Seppälä A, Koskinen K, 2013. Buffer erosion in dilute groundwater. Posiva 2012-44, Posiva Oy.

Schramm L L, Hepler L G, 1994. Surface and interfacial tensions of aqueous dispersions of charged colloidal (clay) particles. Canadian journal of chemistry 72, 1915–1920.

Sena C, Salas J, Arcos D, 2010. Aspects of geochemical evolution of the SKB near field in the frame of SR-Site. SKB TR-10-59, Svensk Kärnbränslehantering AB.

SKB, 2004. Interim process report for the safety assessment SR-Can. SKB R-04-33, Svensk Kärnbränslehantering AB.

SKB, 2006. Long-term safety for KBS-3 repositories at Forsmark and Laxemar – a first evaluation. Main report of the SR-Can project. SKB TR-06-09, Svensk Kärnbränslehantering AB.

SKB, 2011. Long-term safety for the final repository for spent nuclear fuel at Forsmark. Main report of the SR-Site project. SKB TR-11-01, Svensk kärnbränslehantering AB.

Smith P, Schatz T, Reijonen H, Hellä P, 2017. Chemical erosion and mass redistribution of bentonite in a KBS-3H repository. Posiva 2016-12, Posiva Oy.

Vowell S, 2009. Microfluidics effects of surface tension. Available at: http://citeseerx.ist.psu.edu/viewdoc/download?doi=10.1.1.509.7902&rep=rep1&type=pdf

Appendix A

The equations of the KTH model corresponding to the derivation of the smectite diffusion coefficient (Liu et al. 2009), which have been implemented in COMSOL, are presented below:

$$\partial_t \varphi = -\vec{u}\nabla\varphi + \nabla \cdot (D_F \nabla\varphi) \quad \text{Equation A-1}$$

$$D_F = \frac{\chi(1-\varphi)^{1.6}}{f} \quad \text{Equation A-2}$$

$$h = \left(\frac{\varphi_{max}}{\varphi} - 1\right)\delta_p \quad \text{Equation A-3}$$

$$f = \left[6\pi\eta_w r_{eq} + V_p k_0 \tau^2 a_p^2 \eta_w \frac{\varphi}{(1-\varphi)^2}\right] \quad \text{Equation A-4}$$

$$\chi = k_B T + \left(h + \delta_p\right)^2 \left(\frac{\partial F_A}{\partial h} - \frac{\partial F_R}{\partial h}\right) \quad \text{Equation A-5}$$

$$\frac{\partial F_A}{\partial h} = -\frac{A_H S_p}{2\pi}\left[h^{-4} - 2\left(h + \delta_p\right)^{-4} + \left(h + 2\delta_p\right)^{-4}\right] \quad \text{Equation A-6}$$

$$\frac{\partial F_R}{\partial h} = -4\kappa c R T S_p \tanh y^m \left[\cosh y_\infty^m \sinh\left(\frac{y_\infty^m}{2}\right) + \frac{1}{\kappa h}\sinh y_\infty^h + \frac{2}{(\kappa h)^2}\sinh\left(\frac{y_\infty^h}{2}\right)\right] \quad \text{Equation A-7}$$

$$y^m = \operatorname{asinh}\left[2\sinh y_\infty^m + \frac{4}{\kappa h}\sinh\left(\frac{y_\infty^h}{2}\right)\right] \quad \text{Equation A-8}$$

$$y_\infty^m = 4\operatorname{atanh}\left[\tanh\left(\frac{y_\infty^0}{4}\right)\exp\left(-\frac{\kappa h}{2}\right)\right] \quad \text{Equation A-9}$$

$$y_\infty^h = 4\operatorname{atanh}\left[\tanh\left(\frac{y_\infty^0}{4}\right)\exp(-\kappa h)\right] \quad \text{Equation A-10}$$

$$\kappa = \left(\frac{2F^2 c z^2}{\varepsilon_0 \varepsilon_r R T}\right)^{1/2} \quad \text{Equation A-11}$$

$$y_\infty^0 = 2\operatorname{asinh}\left(\frac{s_0}{2}\right) \quad \text{Equation A-12}$$

$$s_0 = \frac{zF\sigma^0}{\varepsilon_0 \varepsilon_r \kappa R T} \quad \text{Equation A-13}$$

The smectite sol viscosity correlation presented by Adachi et al. (1998) has also been implemented:

$$\eta_{rel} = 1 + 1.022\varphi_{cov} + 1.358\varphi_{cov}^3 \quad \text{Equation A-14}$$

$$\varphi_{cov} = \frac{2}{3}\frac{\left(D_P + 2m\kappa^{-1}\right)^3}{D_p^2 \delta_p} \quad \text{Equation A-15}$$

Notation	Property	Value and/or unit
k_B	Boltzmann's constant	1.380×10^{-23} J/K
r_{eq}	Equivalent radius of non-spherical particles	63.66 nm
F	Faraday's constant	96 485 C/mol
m	Fitting parameter in co-volume fraction	1
R	Gas constant	8.314 J/(K mol)
A_H	Hamaker constant	2.5 $k_B T$
$k_0\tau^2$	Kozeny's constant	5, 13
φ_{max}	Maximum volume fraction of smectite	1
ε_0	Permittivity of vacuum	8.854×10^{-12} F/m
ε_r	Relative permittivity of water	78.54
D_p	Smectite particle diameter	200 nm
δ_p	Smectite particle thickness	1 nm
a_p	Specific surface area per unit volume of particles	$2/\delta_p$ m^2/m^3
S_p	Surface area of smectite particle	3.1415×10^{-14} m^2
σ^0	Surface charge of particles	−0.131 C/m^2
T	Temperature	298.15 K
z	Valence of counterion	1
η_w	Viscosity of water	1.002×10^{-3} N s/m^2
φ	Volume fraction of smectite – variable	-
V_p	Volume of the smectite particles	3.1415×10^{-23} m^3

Appendix B

In the present case, according to Schramm and Hepler (1994), a relevant force is expected to appear at the interface between dilute gel and seeping water due to the surface tension differential, which has been measured in 2 $mN \cdot m^{-1}$. In this sense, Girifalco and Good (1957) provided the following analytical expression of the interfacial tension σ_{int} ($N \cdot m^{-1}$) between two liquid phases *a* and *b*:

$$\sigma_{int} = \sigma_a + \sigma_b - 2\Phi\sqrt{\sigma_a \sigma_b} \qquad \text{Equation B-1}$$

This tension is very sensitive to the parameter Φ, which has been estimated for liquid-solid interfaces but has not been properly defined for liquid-liquid interactions (Jańczuk et al. 1996). Then, the resulting stress on the outer surface of the sol τ_{fric} (Pa) would be:

$$\tau_{fric} = \tau_1 + \frac{2\sigma_{int}}{\delta} \qquad \text{Equation B-2}$$

Appendix C

An alternative form of the wall friction term presented in Section 4.4.2 is being currently evaluated. It is based on the same physical assumptions and no fundamental differences are expected to appear in the results. However, the derivation of the numerical model does not link the shear resistance of the smectite flocs accumulating at the rim to a new volume term in the expansion equation. Instead, the model links it to a boundary condition. As shown in Figure 6-5, the added conservative convective term in the original formulation is only relevant at the vicinity of the rim, although it is applied overall in the fracture as a volume term (Equation C-1).

$$\partial_t \varphi + \vec{u} \cdot \nabla \varphi + \nabla \cdot (\vec{w} \varphi) - \nabla \cdot (D \nabla \varphi) = 0 \qquad \text{Equation C-1}$$

Since Equation C-1 is to be solved with the finite element method (FEM), its weak form must be derived (Equation C-2), which yields:

$$(\psi, \partial_t \varphi)_\Omega + (\psi, \vec{u} \cdot \nabla \varphi)_\Omega + (\psi, \nabla \cdot (\vec{w} \varphi))_\Omega - (\psi, \nabla \cdot (D \nabla \varphi))_\Omega = 0 \qquad \text{Equation C-2}$$

with Ω being the whole domain (the wall friction velocity $\vec{w}$ is set to zero inside the bentonite pellet or buffer). If the wall friction and the diffusive terms (third and fourth terms, respectively) are integrated by parts the natural boundary condition on the domain outer boundaries (Γ) (Neumann fluxes) arise (last term in Equation C-3):

$$(\psi, \partial_t \varphi)_\Omega + (\psi, \vec{u} \cdot \nabla \varphi)_\Omega - (\nabla \psi, \vec{w} \varphi)_\Omega + (\nabla \psi, D \nabla \varphi)_\Omega + (\psi, (\vec{w} \cdot \vec{n}) \varphi - D \nabla \varphi \cdot \vec{n})_\Gamma = 0 \qquad \text{Equation C-3}$$

As the outer boundaries lay in general far away from the expanding disc (Figure C-1a), these fluxes will be negligible, and this term will not be considered.

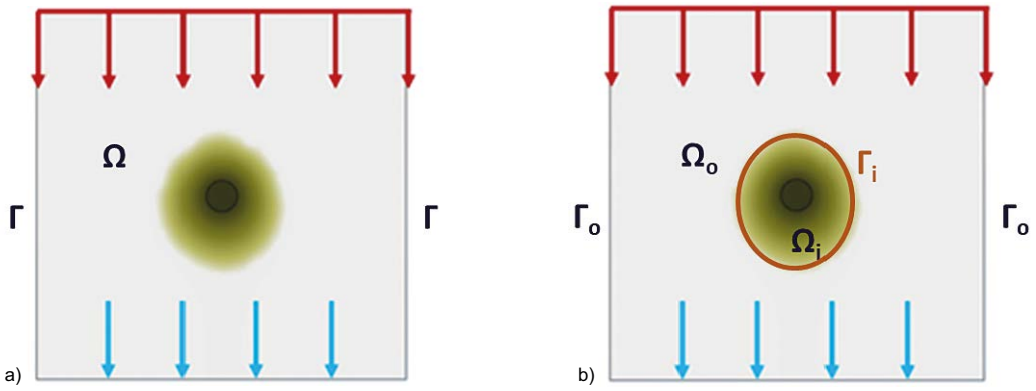

Figure C-1. *Computational domains for the first model (a) and the second model (b).*

However, this approach leads to two issues that deserve to be briefly discussed. First, the addition of a new convective term affects the convergence of the solver, thus significantly increasing the computational cost. At a conceptual level, the previous approach applies the wall friction term to the expansive bulk, although it is only effective near the rim. One could think about applying this counter-force against expansion as a boundary condition imposed on the rim without the necessity of an extra term as in Equation C-1. If the original smectite transport equation presented by Liu et al. (2009) is considered, the weak form in Equation C-2 is reduced to:

$$(\psi, \partial_t \varphi)_\Omega + (\psi, \vec{u} \cdot \nabla \varphi)_\Omega - (\psi, \nabla \cdot (D \nabla \varphi))_\Omega = 0 \qquad \text{Equation C-4}$$

If the second order diffusive term in Equation C-4 is integrated by parts and the domain Ω is decomposed into an inner expanding domain (Ω_i) and an outer passive domain (Ω_o) with the interface Γ_i in between (rim), Equation C-5 is obtained:

$$(\psi, \partial_t \varphi)_\Omega + (\psi, \vec{u} \cdot \nabla \varphi)_\Omega + (\nabla \psi, D \nabla \varphi)_\Omega - (\psi,\ D \nabla \varphi \cdot \vec{n})_{\Gamma i} = 0 \qquad \text{Equation C-5}$$

The last step consists in modelling the natural boundary condition at the rim (last term in Equation C-5). The flux at the rim should correspond to the shear stress exerted by the segregated material against the advance of the expanding paste in Ω_i. For this reason, the advective flux obtained in Equation C-3 is prescribed on Γ_i:

$$(\psi, \partial_t \varphi)_\Omega + (\psi, \vec{u} \cdot \nabla \varphi)_\Omega + (\nabla \psi, D \nabla \varphi)_\Omega + (\psi,\ (\vec{w} \cdot \vec{n}) \varphi)_{\Gamma i} = 0 \qquad \text{Equation C-6}$$

Preliminary calculations show a considerable reduction of the computational cost (from 1–2 days to 1–2 hours). This is a remarkable improvement if one takes into account that an extra equation for the moving mesh must be solved. The interface Γ_i will be forced to move outwards with a radial velocity defined by the balance between the maximum diffusive flux extruding the paste and the blocking advective flux corresponding to the wall friction term (Equation C-7).

$$u_{rim} = \max_{\Omega}(D \nabla \varphi \cdot \vec{n}) - \varphi \vec{w} \cdot \vec{n} \qquad \text{Equation C-7}$$

As a result, the mesh nodes will move at a certain velocity ($\vec{u}_{\text{mesh}}$) in order to absorb the deformation of the elements. This requires the use of an Arbitrary Lagrangian Eulerian (ALE) frame of reference, which instead of evaluating the equations in a fixed reference allows it to have an arbitrary motion, in the present case the mesh velocity (Equation C-8).

$$(\psi, \partial_t \varphi)_\Omega + (\psi, (\vec{u} - \vec{u}_{mesh}) \cdot \nabla \varphi)_\Omega + (\nabla \psi, D \nabla \varphi)_\Omega + (\psi,\ (\vec{w} \cdot \vec{n}) \varphi)_{\Gamma i} = 0 \qquad \text{Equation C-8}$$

One issue to be addressed in this approach is the interference between the wall friction boundary condition at the rim and flow erosion. It must still be clarified whether the protective effect of accumulated flocculation against water carrying colloids away from the rim, which has been observed experimentally, can be properly described by the model or not.

Appendix D

Cases 7 and 8 (Table 3-1) simulate two experimental tests performed respectively by Magnus Hedström at Clay Technology AB laboratory in Sweden and by A-Insinöörit Civil Oy laboratory in Finland (both unpublished work), which have been developed in collaboration with Posiva. These tests are briefly presented in this appendix. Case 7 corresponds to Test 2 in this appendix, while case 8 to Test 5.

Their main objective was to evaluate the performance and robustness of a measurement system for studying clay mineral erosion in artificial factures under flowing synthetic groundwater conditions. Several tests in different setups were performed to reproduce the conditions that might reduce dry density of bentonite.

The two tests studied here (denoted as Test 2 and Test 5) were conducted with an artificial fracture setup with an annular sample compartment at the centre of the test cell. Thus, swelling in these tests is radial. The clay was homoionic Na-montmorillonite with initial nominal dry density of 1 420 kg/m^3 in Test 2 and 1 100 kg/m^3 in Test 5. The samples were placed in a specimen cylindrical compartment with 20 mm in diameter. The test cells were placed vertically, and the flow of 1 mM NaCl solution was imposed from top to bottom (maintained constant with a peristaltic pump). The solution was prepared using deaerated and deionized water. Some initial air pockets were observed, that subsequently disappeared due to the constant flow of deaerated solution. The solution was shielded from the atmosphere by means of collapsible containers (Hydra-Pak Shape-shiftTM) to avoid lowering of pH from the interaction with atmospheric CO_2. More details about the experiments are included in Table 3-1 and in Section 6.3.3 and 6.3.4.

The tests ran for a period of 63 days and upon termination two main results were obtained: a limited expansion radius of approximately 24 mm in Test 2 and 8.9 mm in Test 5, and an early decrease of the erosion rate of Test 2 leading to a 2 % of accumulated mass loss at the bottom of the fracture. This apparently reduced mass loss was tightly related to the partial clogging of the fracture due to the coagulation of smectite flocs in the form of a secondary gel.

Arkitektkopia AB, Bromma, 2022

A CO-OPERATION REPORT BETWEEN SVENSK KÄRNBRÄNSLEHANTERING AB AND POSIVA OY

SKB's and Posiva's programmes both aim at the disposal of spent nuclear fuel based on the KBS-3 concept. Formal cooperation between the companies has been in effect since 2001. In 2014 the companies agreed on extended cooperation where SKB and Posiva share the vision "Operating optimised facilities in 2030". To further enhance the cooperation, Posiva and SKB started a series of joint reports in 2016, which includes this report.